



# Electrochemical Transport Phenomena in Hybrid Pseudocapacitors under Galvanostatic Cycling

Anna L. d'Entremont, Henri-Louis Girard, Hainan Wang, and Laurent Pilon<sup>\*,z</sup>

Henry Samueli School of Engineering and Applied Science, Mechanical and Aerospace Engineering Department, University of California, Los Angeles, Los Angeles, California 90095, USA

This study aims to provide insights into the electrochemical transport and interfacial phenomena in hybrid pseudocapacitors under galvanostatic cycling. Pseudocapacitors are promising electrical energy storage devices for applications requiring large power density. They also involve complex, coupled, and multiscale physical phenomena that are difficult to probe experimentally. The present study performed detailed numerical simulations for a hybrid pseudocapacitor with planar electrodes and binary, asymmetric electrolyte under various cycling conditions, based on a first-principles continuum model accounting simultaneously for charge storage by electric double layer (EDL) formation and by faradaic reactions with intercalation. Two asymptotic regimes were identified corresponding to (i) dominant faradaic charge storage at low current and low frequency or (ii) dominant EDL charge storage at high current and high frequency. Analytical expressions for the intercalated ion concentration and surface overpotential were derived for both asymptotic regimes. Features of typical experimentally measured cell potential were physically interpreted. These insights could guide the optimization of hybrid pseudocapacitors.

© The Author(s) 2015. Published by ECS. This is an open access article distributed under the terms of the Creative Commons Attribution Non-Commercial No Derivatives 4.0 License (CC BY-NC-ND, <http://creativecommons.org/licenses/by-nc-nd/4.0/>), which permits non-commercial reuse, distribution, and reproduction in any medium, provided the original work is not changed in any way and is properly cited. For permission for commercial reuse, please email: [oa@electrochem.org](mailto:oa@electrochem.org). [DOI: 10.1149/2.0441602jes] All rights reserved.

Manuscript submitted September 14, 2015; revised manuscript received November 2, 2015. Published November 18, 2015.

Electrochemical capacitors (ECs) are promising electrical energy storage devices for applications requiring large power density, rapid response, and/or long cycle life.<sup>1-3</sup> They can be divided into two categories, namely electric double layer capacitors (EDLCs) and pseudocapacitors. Both types of devices consist of two porous electrodes on either side of a separator impregnated with electrolyte. EDLCs store electric charge within the electric double layer (EDL) consisting of a layer of electronic charge at the surface of the electrode and an oppositely charged layer of ions in the electrolyte.<sup>1,4</sup> Pseudocapacitors combine the energy storage mechanisms used in batteries with those used in EDLCs by storing electric charge chemically via redox reactions and electrostatically within the EDL.<sup>1,4,5</sup> The electrical performance of pseudocapacitors closely resembles that of EDLCs rather than that of batteries despite their use of faradaic charge storage.<sup>1,5,6</sup> In fact, an ideal battery operates at a constant cell potential independent of its state of charge (SOC), whereas the cell potential of an EDLC or a pseudocapacitor varies continuously with its SOC.<sup>3</sup> Finally, hybrid or asymmetric pseudocapacitors can be designed by pairing a redox-active or pseudocapacitive electrode (e.g., TiO<sub>2</sub>, MnO<sub>2</sub>, Nb<sub>2</sub>O<sub>5</sub>) with an EDLC-type electrode made of carbon.<sup>3</sup> In general, electrochemical capacitors exhibit electrical performance between that of batteries and that of dielectric capacitors.<sup>1-3</sup> They typically have larger power densities, cycle life, and cycle efficiencies than batteries as well as much larger energy densities than dielectric capacitors.<sup>2</sup> Among electrochemical capacitors, pseudocapacitors yield larger capacitances and energy densities than EDLCs because they combine faradaic and EDL charge storage and can accommodate more charge per unit electrode surface area and volume than EDL charge storage alone.<sup>3,5-7</sup>

Pseudocapacitors involve complex, coupled, and multiscale electrochemical transport and interfacial phenomena that are difficult to monitor experimentally. For example, it is difficult to discriminate between the fraction of charge storage achieved from faradaic reactions and that from EDL formation. Experimentalists have attempted to differentiate between surface-controlled processes, such as EDL capacitance, and diffusion-controlled processes, such as battery-like faradaic charge storage with intercalation. To do so, they analyzed the relationship between the amount of charge stored (called the "capacity" in C or in mAh) or the current and the scan rate in cyclic voltammetry (CV) measurements.<sup>7-9</sup> However, this analysis was derived from the behavior associated with EDL and faradaic charge

storage occurring independently of each other.<sup>6</sup> In practice, EDL formation and redox reactions can take place simultaneously, making it difficult to interpret experimental results for pseudocapacitors. Note also that, to the best of our knowledge, this analysis method is specific to CV and cannot be used for galvanostatic cycling.

The present study aims to investigate and to physically interpret the detailed electrochemical transport behavior in hybrid pseudocapacitors under galvanostatic cycling. Particular attention was paid to determining the respective contributions of EDL formation and faradaic reactions to energy storage under various cycling conditions and to identifying the physical phenomena limiting the faradaic charge storage. These insights were used to physically interpret features of experimentally measured cell potentials, and could help guide optimization of hybrid pseudocapacitor designs, materials, and operating conditions. To accomplish these objectives, detailed numerical simulations were performed for a hybrid pseudocapacitor using a first-principles continuum model predicting the spatiotemporal evolution of the electric potential and concentrations.<sup>10</sup>

## Background

**Capacitance.**— The capacitance of an electrochemical capacitor characterizes the amount of electric charge  $q_s$  (in C) stored from the external circuit as a function of the cell potential  $\psi_s$  (in V). The areal capacitance  $C_s$  is defined as the capacitance per unit electrode/electrolyte interfacial area, expressed in F m<sup>-2</sup>. The differential  $C_{s,diff}$  and the integral  $C_{s,int}$  areal capacitances can be determined by galvanostatic cycling at constant current density  $\pm j_s = dq_s/dt$  according to Refs. 1,11

$$C_{s,diff} = \frac{dq_s}{d\psi_s} = \frac{j_s}{|d\psi_s/dt|} \quad \text{and} \quad C_{s,int} = \frac{q_s}{\psi_s} = \frac{j_s t_c / 2}{\psi_{max} - \psi_{min}} \quad [1]$$

where  $\psi_{max}$  and  $\psi_{min}$  are the upper and lower limits of  $\psi_s(t)$ , and  $t_c$  is the cycle period (in s).

**Experimental studies of pseudocapacitive materials.**— Various transition metal oxides have shown promising pseudocapacitive performance.<sup>6,12</sup> For example, recent studies have demonstrated large capacitance associated with Li<sup>+</sup> intercalation into crystalline Nb<sub>2</sub>O<sub>5</sub>.<sup>7,8,12-14</sup> In hybrid Nb<sub>2</sub>O<sub>5</sub>/activated carbon pseudocapacitors, the Nb<sub>2</sub>O<sub>5</sub> electrode typically serves as the negative electrode relative

\*Electrochemical Society Active Member.

<sup>z</sup>E-mail: [pilon@seas.ucla.edu](mailto:pilon@seas.ucla.edu)

to the positive activated carbon electrode.<sup>8,12,14</sup> This corresponds to  $\text{Li}^+$  intercalation in the  $\text{Nb}_2\text{O}_5$  electrode during charging and deintercalation during discharging. It is interesting to note that the synthesis of  $\text{Nb}_2\text{O}_5$  described in Ref. 13 resulted in  $\text{Nb}_2\text{O}_5$  electrodes with no initial Li and minimal contaminants, based on X-ray photoelectron spectroscopy data.<sup>13</sup>

Pseudocapacitance has also been demonstrated with  $\text{MnO}_2$  involved in reversible redox reactions with  $\text{H}^+$ ,  $\text{K}^+$ , and  $\text{Li}^+$ .<sup>15–19</sup> In contrast to  $\text{Nb}_2\text{O}_5$ ,  $\text{MnO}_2$  has typically been used as the positive electrode in hybrid pseudocapacitors.<sup>15</sup> This corresponds to charging the device by deintercalation of the cation. Then, the pseudocapacitive electrode must contain a significant concentration of the reduced cation at the beginning of the cycle. Indeed, several pseudocapacitor studies, featuring  $\text{MnO}_2$  electrodes reacting with  $\text{K}^+$ , synthesized pseudocapacitive  $\text{MnO}_2$  electrodes by reduction of  $\text{KMnO}_4$ ,<sup>16–18</sup> resulting in the initial electrode composition  $\text{K}_{0.02}\text{MnO}_2\text{H}_{0.33}$ .<sup>16</sup> This corresponded to an initial concentration of K in the pseudocapacitive electrode of around  $1 \text{ mol L}^{-1}$ . Similarly, a study considering pseudocapacitors with  $\text{Li}^+$  intercalation into  $\text{MnO}_2$  synthesized the pseudocapacitive electrodes by reacting  $\text{MnO}_2$  with  $\text{Li}_2\text{CO}_3$  to obtain the initial composition  $\text{Li}_{0.5}\text{MnO}_2$ ,<sup>19</sup> i.e., an initial Li concentration around  $30 \text{ mol L}^{-1}$ .

For experiments under galvanostatic cycling, the cell potential  $\psi_s(t)$  is typically reported as a function of time. EC cell potentials are typically computed as the potential of the electrode giving up electrons to the external circuit during charging relative to that receiving electrons. Thus, the cell potential  $\psi_s(t)$  increases during charging and decreases during discharging. Figure 1 shows some typical examples of cell potential  $\psi_s(t)$  as a function of time for hybrid pseudocapacitors featuring (a) a  $\text{Nb}_2\text{O}_5$  negative electrode reacting with  $\text{Li}^+$ <sup>12</sup> or (b) a  $\text{MnO}_2$  positive electrode reacting with  $\text{K}^+$ .<sup>20</sup> Figure 1a indicates that, for hybrid pseudocapacitors with  $\text{Nb}_2\text{O}_5$ , the cell potential  $\psi_s(t)$  increased rapidly at the beginning of the charging step.<sup>9,12,21</sup> Then, the rate of change  $|\text{d}\psi_s/\text{d}t|$  abruptly decreased, resulting in a distinct “kink” in the potential evolution. The slope  $|\text{d}\psi_s/\text{d}t|$  also increased toward the end of the cycle, although it was not as large as at the beginning of the cycle. The cell potential  $\psi_s$  varied approximately linearly for the rest of the cycle, except for a very brief period of large slope  $|\text{d}\psi_s/\text{d}t|$  immediately after the charging/discharging transition.<sup>9,12,21</sup>

Figure 1a also shows experimentally measured potential drops between each electrode and a reference electrode, denoted as  $\Delta\psi_P(t)$  and  $\Delta\psi_C(t)$  for the pseudocapacitive and carbon electrodes, respectively, and such that  $\psi_s(t) = \Delta\psi_C(t) - \Delta\psi_P(t)$ . It indicates that  $\Delta\psi_C(t)$  for the carbon electrode varied linearly and that the variation of  $|\text{d}\psi_s/\text{d}t|$  was associated with the pseudocapacitive electrode. Note that the range of  $\Delta\psi_P(t)$  and of  $\Delta\psi_C(t)$ , and thus the integral capacitances of the individual electrodes, were of the same order of magnitude. This can be attributed to the fact that the carbon electrode’s mass loading was 4.7 times that of the  $\text{Nb}_2\text{O}_5$  electrode, ensuring that both electrodes had the same capacitance at a particular current density.<sup>12</sup> Indeed, it is common for hybrid pseudocapacitors to have electrodes with different loadings in order to match their capacitances.<sup>9,18–22</sup> Figure 1b indicates that, for hybrid pseudocapacitors featuring  $\text{MnO}_2$  positive electrodes,  $\psi_s(t) = \Delta\psi_P(t) - \Delta\psi_C(t)$  varied approximately linearly through most of the cycle. There was a slightly larger slope  $|\text{d}\psi_s/\text{d}t|$  immediately after the charging/discharging transition. Finally, pseudocapacitors and EDLCs with large electrical resistance and/or cycled at large currents also featured IR drops corresponding to instantaneous jumps in  $\psi_s$  at the transitions between charging and discharging steps and given by Ohm’s law. The present study aims to numerically reproduce these typical experimental curves in order to interpret their features.

**Electric double layer structure.**— Figure 2a illustrates the electric double layer (EDL) structure of a binary and asymmetric electrolyte near a planar pseudocapacitive electrode according to the Stern model.<sup>23,24</sup> The EDL is the region close to the electrode/electrolyte interface with a non-zero space charge density, whereas the bulk electrolyte remains electrically neutral. The net ionic charge in the EDL

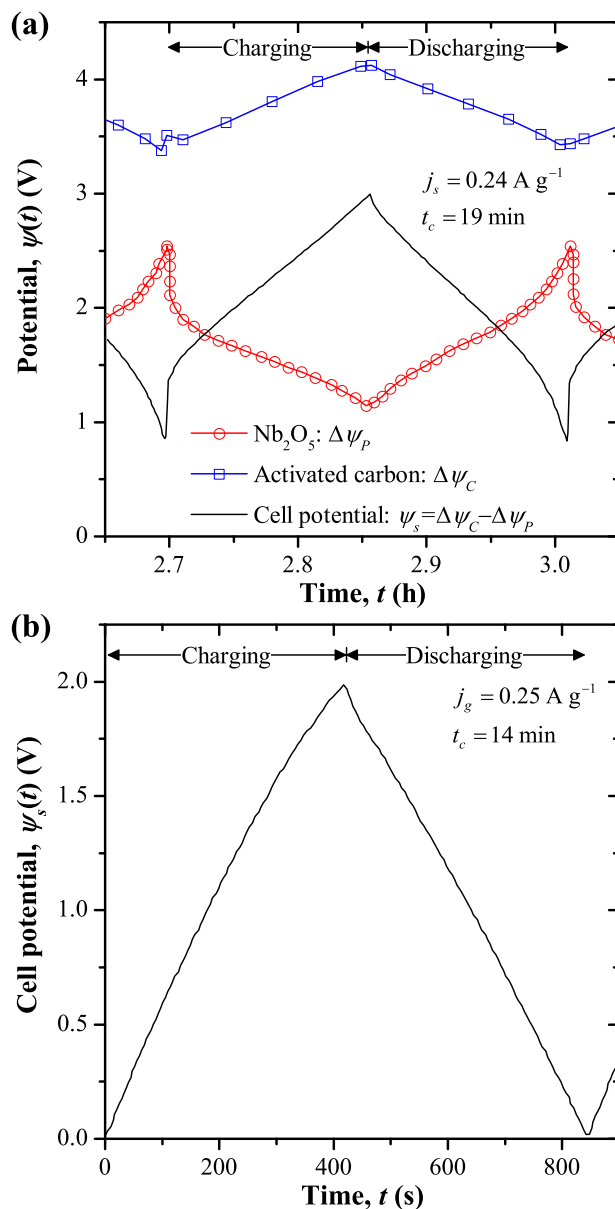


**Figure 1.** Characteristic examples of the experimental (a) potential drops between each electrode and a reference electrode,  $\Delta\psi_P(t)$  for the pseudocapacitive electrode and  $\Delta\psi_C(t)$  for the carbon electrode as well as the cell potential  $\psi_s(t) = \Delta\psi_C(t) - \Delta\psi_P(t)$  for a hybrid pseudocapacitor featuring  $\text{Nb}_2\text{O}_5$  reacting with  $\text{Li}^+$ <sup>12</sup> and (b) cell potential  $\psi_s(t) = \Delta\psi_P(t) - \Delta\psi_C(t)$  for a hybrid pseudocapacitor featuring a positive  $\text{MnO}_2$  electrode reacting with  $\text{K}^+$ <sup>20</sup> as functions of time  $t$ .

per unit electrode/electrolyte interfacial area (in  $\text{C m}^{-2}$ ) is equal and opposite to the net electronic surface charge density in the electrode to maintain overall electroneutrality of the interfacial region.<sup>4,23–25</sup> The electrolyte can be divided into the Stern and the diffuse layers. The Stern layer is the compact layer adjacent to the electrode surface and containing no free charge.<sup>23,24</sup> The Stern/diffuse layer interface marks the closest distance of approach for a solvated ion.<sup>25</sup> Within the diffuse layer, ions are mobile under the competing influences of electrostatic forces, diffusion, and steric repulsion.<sup>23,24,26</sup>

**Models of electrochemical capacitors.**— Various models have been proposed for the electrochemical behavior of pseudocapacitors. Several studies have employed equivalent RC circuit models composed of ideal resistors and capacitors.<sup>27–31</sup> The values of resistances

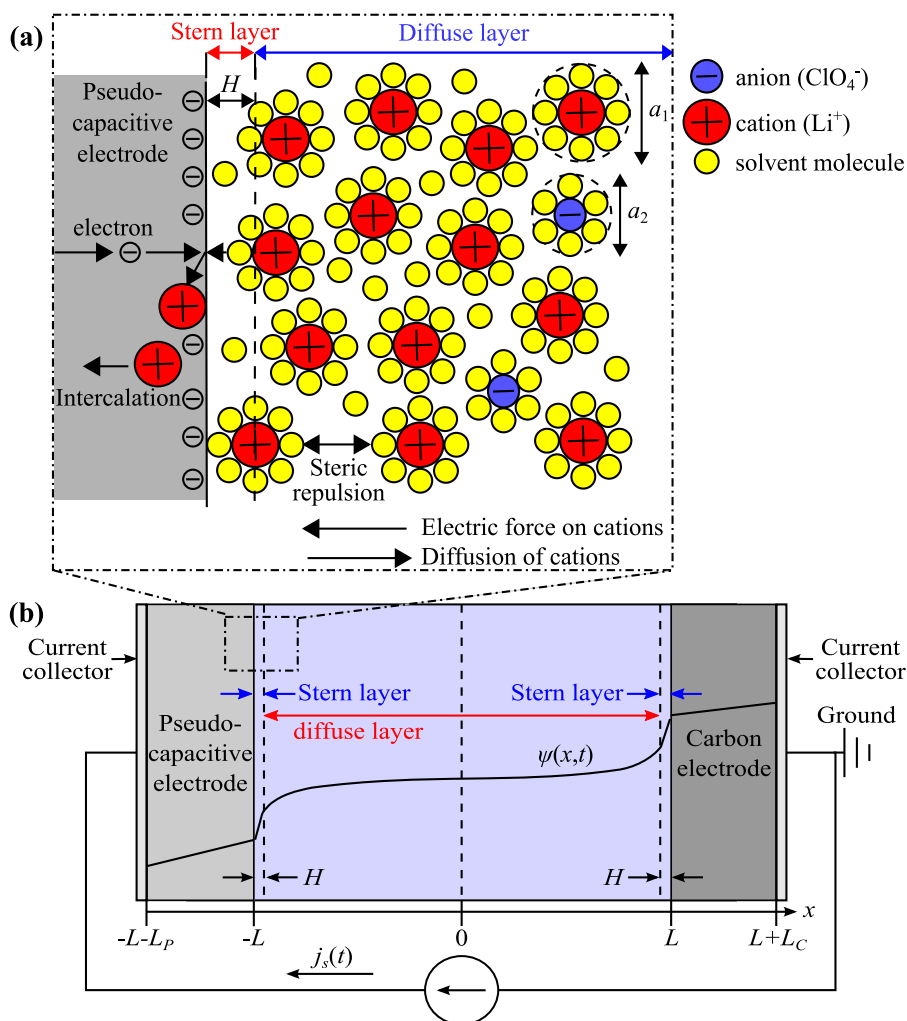


**Figure 2.** Illustration of (a) the electric double layer structure of a binary and asymmetric electrolyte with redox reactions near a planar electrode and (b) the simulated hybrid pseudocapacitor with planar electrodes, along with the associated coordinate system.

and capacitances used in such models were fitted from experimental data. RC circuit models can be used for control purposes but, unfortunately, provide little insight into the physical phenomena governing pseudocapacitor operation.<sup>32</sup> In addition, many were developed under the assumption of uniform electrolyte concentration and cannot adequately account for EDL formation.<sup>33–35</sup>

Other proposed models for pseudocapacitors solved the Poisson equation governing local electric potential,<sup>10,36–41</sup> sometimes coupled with the mass transport equation governing the ion concentrations in the electrolyte.<sup>10,37,38</sup> Most of these models considered porous electrodes as homogeneous composites with some effective electrical conductivity<sup>36–41</sup> and effective ion diffusion coefficients.<sup>37,38</sup> They were used to investigate the effects of pseudocapacitive electrode morphology,<sup>36,37,42</sup> exchange current density,<sup>39,40</sup> and EDL areal capacitance<sup>40</sup> on the temporal evolution of the cell potential during discharging as well as the energy and power densities under galvanostatic operation. Some studies also focused on tool development for simulating stacks of many pseudocapacitor cells with relatively low computational cost<sup>38</sup> or for retrieving cell properties such as the electrical conductivity of the electrode or electrolyte, the EDL capacitance, and/or the exchange current density from experimental measurements.<sup>40</sup> Such models are valuable for simulating entire devices with porous electrodes of realistic dimensions. However, they often accounted for the EDL formation only via a constant EDL capacitance<sup>36–41</sup> taken from experimental measurements for carbon<sup>36,37,41</sup> or used as a fitting parameter.<sup>38</sup> They also typically assumed that the ion concentrations in the electrolyte were uniform,<sup>36,39–42</sup> treated ions as point charges,<sup>37,38</sup> and/or accounted

only for ion diffusion while ignoring electromigration.<sup>37</sup> In other words, the two charge storage mechanisms, i.e., EDL formation and redox reactions, were entirely decoupled. Recently, we presented a continuum model accounting simultaneously for coupled EDL formation and faradaic reactions and for finite ion size.<sup>10</sup> This model was used to physically interpret cyclic voltammetry (CV) measurements for hybrid pseudocapacitors with planar electrodes and binary and asymmetric electrolyte.<sup>10</sup> The study established that CV curves featured a faradaic regime dominated by redox reactions and a capacitive regime dominated by EDL formation. It also clarified the physical interpretation of the so-called “*b*-value” observed experimentally in the power law relating current and scan rate.<sup>10</sup>

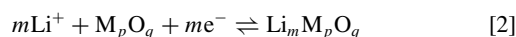
Finally, molecular dynamics (MD) and density functional theory (DFT) models, accounting for individual atoms and their interactions, have also been developed for pseudocapacitors.<sup>43–48</sup> They have been used to predict the energy barriers associated with surface adsorption and bulk intercalation<sup>43–46</sup> as well as the charge distribution,<sup>44</sup> the diffusion pathways for intercalated ions,<sup>43,48</sup> and the crystal structure of the pseudocapacitive electrode material.<sup>43,44,46,47</sup> Unfortunately, the large computational cost limits MD simulations to time and length scales on the order of 10 nm and 10  $\mu$ s,<sup>49,50</sup> respectively. These are much smaller than realistic device dimensions or time scales for pseudocapacitor charging and discharging under galvanostatic cycling, making MD models impractical for simulating realistic device operation.

The present study investigates and physically interprets the detailed electrochemical transport phenomena in a hybrid pseudocapacitor under galvanostatic cycling. It focuses in particular

on the allocation of stored charge between the EDLs and pseudocapacitive ion intercalation under various operating conditions. To this end, detailed numerical simulations were performed for a planar hybrid pseudocapacitor with binary and asymmetric electrolyte using realistic current densities and potential windows based on a first-principles continuum model.<sup>10</sup> The EDL capacitance was predicted from first principles and the faradaic current density was computed based on the local concentrations and surface overpotential at the Stern/diffuse layer interface. The model predicts the spatiotemporal evolutions of the electric potential, the ion concentrations within the EDLs and bulk electrolyte, and of the concentration of intercalated cations in the pseudocapacitive electrode. It bridges the gap between existing continuum models simulating entire porous electrodes and treating ions as point charges and MD models simulating nanoscale regions. In contrast to most existing continuum models,<sup>36–42</sup> it simultaneously accounts for the coupling between the EDL formation and the faradaic reaction.

### Analysis

*Schematic and assumptions.*—Figure 2b illustrates the one-dimensional (1D) hybrid pseudocapacitor considered in the present study and the associated coordinate system. The simulated device consisted of two current collectors supporting planar electrodes separated by a binary and asymmetric electrolyte with inter-electrode distance  $2L$ . The pseudocapacitive electrode of thickness  $L_P$  consisted of a transition metal oxide  $M_pO_q$  reacting chemically with  $Li^+$  according to the following reversible redox reaction



where  $m$  is the number of  $Li^+$  ions intercalated per molecule of the metal oxide  $M_pO_q$ . Its maximum value depends on the metal oxide. For example,  $Nb_2O_5$  reacting with  $Li^+$  forms  $Li_2Nb_2O_5$  with  $m = 2$  in its fully-lithiated state.<sup>12</sup> The heterogeneous reaction occurring at the pseudocapacitive electrode/electrolyte interface transferred  $Li^+$  ions from the electrolyte into the  $M_pO_q$  matrix.<sup>23–25</sup> Subsequently, the intercalated  $Li^+$  migrated farther into the pseudocapacitive electrode, accompanied by reduction of the transition metal cations.<sup>12,25</sup> On the other hand, the planar carbon electrode of thickness  $L_C$  did not react chemically with the electrolyte. Instead, it stored charge only in the EDL forming near its surface.

To make the problem mathematically tractable, the following assumptions were made: (1) The heterogeneous redox reaction occurred within the Stern layer near the pseudocapacitive electrode. This assumption is commonly used in models of batteries and electrochemical capacitors, since free electrons and free  $Li^+$  ions are assumed to be confined to the electrodes and to the diffuse layer, respectively.<sup>23</sup> (2) Bulk motion of the electrolyte was negligible. (3) Transport of the intercalated species in the pseudocapacitive electrode was treated as a diffusion process. (4) No phase transition occurred in the pseudocapacitive material. This was consistent with experimental observations for  $Nb_2O_5$ .<sup>12</sup> (5) The physicochemical properties of the electrodes and the electrolyte were assumed to be constant. In practice, the electrical conductivity  $\sigma_P$  and the  $Li^+$  diffusion coefficient  $D_{1,P}$  in the pseudocapacitive electrode may change with the concentration of intercalated  $Li^+$ . Similarly, the electrolyte transport properties may change with the local electric field and/or ion concentrations. However, to the best of our knowledge, no quantitative models or experimental measurements for  $\sigma_P$  or  $D_{1,P}$  of metal oxides as a function of intercalated  $Li^+$  concentration exist. (6) The Stern layer thickness  $H$  was identical at both electrodes and equal to half the effective diameter  $a_{i,E}$  of the largest ion species  $i$ , i.e.,  $H = \max(a_{i,E}/2)$ . (7) Non-electrostatic ion adsorption was negligible. In fact, previous simulations of EDLCs using this assumption<sup>51,52</sup> agreed well with experimental data. (8) The potential drop across the current collectors was negligible, so that only the electrodes and the electrolyte were simulated. (9) The cell temperature was uniform and constant, and heat generation was ignored.

*Governing equations.*—*In the electrodes.*—The local electric potential  $\psi(\mathbf{r}, t)$  in each electrode obeys Poisson's equation given by<sup>53</sup>

$$\begin{aligned} \nabla \cdot (\sigma_P \nabla \psi) &= 0 && \text{in the pseudocapacitive electrode} \\ \text{and } \nabla \cdot (\sigma_C \nabla \psi) &= 0 && \text{in the carbon electrode} \end{aligned} \quad [3]$$

where  $\sigma_P$  and  $\sigma_C$  are the electrical conductivities of the pseudocapacitive and carbon electrode materials, respectively. The spatiotemporal evolution of the local concentration  $c_{1,P}(\mathbf{r}, t)$  of intercalated lithium ions in the pseudocapacitive electrode is governed by the mass diffusion equation written as<sup>54–56</sup>

$$\frac{\partial c_{1,P}}{\partial t} = -\nabla \cdot \mathbf{N}_{1,P} \quad \text{with } \mathbf{N}_{1,P} = -D_{1,P} \nabla c_{1,P}. \quad [4]$$

Here,  $\mathbf{N}_{1,P}$  is the molar flux vector given by Fick's law (in  $\text{mol m}^{-2}\text{s}^{-1}$ ) and  $D_{1,P}$  is the diffusion coefficient (in  $\text{m}^2\text{s}^{-1}$ ) of intercalated  $Li^+$  inside the pseudocapacitive material. Note that lithium intercalation did not take place in the carbon electrode assumed to be chemically inert.

*In the electrolyte.*—The generalized modified Poisson-Nernst-Planck (GMPNP) model<sup>57</sup> can be used to predict the local electric potential  $\psi(\mathbf{r}, t)$  and ion concentrations  $c_{i,E}(\mathbf{r}, t)$  of ion species  $i$  in the electrolyte. It accounts for finite ion size and is applicable to multi-species and asymmetric electrolytes, i.e., electrolytes with more than two ion species and/or having different valencies  $z_{i,E}$ , effective ion diameters  $a_{i,E}$ , and/or diffusion coefficients  $D_{i,E}$ .<sup>57</sup> The electric potential  $\psi(\mathbf{r}, t)$  in the electrolyte is governed by Poisson's equation expressed, for a binary electrolyte ( $i = 1$  or  $2$ ), as<sup>57</sup>

$$-\nabla \cdot (\epsilon_0 \epsilon_r \nabla \psi) = \begin{cases} 0 & \text{in the Stern layers} \\ F \sum_{i=1}^2 z_{i,E} c_{i,E} & \text{in the diffuse layer} \end{cases} \quad [5]$$

where  $\epsilon_0 = 8.854 \times 10^{-12} \text{ F m}^{-1}$  and  $\epsilon_r$  are the vacuum permittivity and the relative permittivity of the electrolyte, respectively. The Faraday constant is denoted by  $F = 96485 \text{ C mol}^{-1}$ . The local ion concentration  $c_{i,E}(\mathbf{r}, t)$  in the diffuse layer is governed by the mass conservation equation<sup>57</sup>

$$\frac{\partial c_{i,E}}{\partial t} = -\nabla \cdot \mathbf{N}_{i,E} \quad \text{with } i = 1 \text{ or } 2 \quad [6]$$

where  $\mathbf{N}_{i,E}$  is the molar flux (in  $\text{mol m}^{-2}\text{s}^{-1}$ ) of ion species  $i$  in the electrolyte expressed as<sup>57</sup>

$$\begin{aligned} \mathbf{N}_{i,E} &= -D_{i,E} \nabla c_{i,E} - \frac{D_{i,E} z_{i,E} F c_{i,E}}{R_u T} \nabla \psi \\ &\quad - \frac{D_{i,E} c_{i,E} N_A}{1 - N_A \sum_{j=1}^2 a_{j,E}^3 c_{j,E}} \sum_{j=1}^2 a_{j,E}^3 \nabla c_{j,E}. \end{aligned} \quad [7]$$

Here,  $T$  is the local absolute temperature (in K),  $N_A = 6.022 \times 10^{23} \text{ mol}^{-1}$  is the Avogadro constant, and  $R_u = 8.314 \text{ J K}^{-1} \text{ mol}^{-1}$  is the universal gas constant. The first and second terms on the right-hand side of Equation 7 represent fluxes due to diffusion and electromigration, respectively, while the third term accounts for steric effects.<sup>57</sup> In particular, the steric term prevents the ion concentration from exceeding the theoretical maximum concentration  $c_{i,E,max} = 1/N_A a_{i,E}^3$  corresponding to simple cubic packing of spherical ions.

*The faradaic current density.*—The transport processes in the pseudocapacitive electrode and in the electrolyte are coupled with the faradaic reaction occurring at their interface. The faradaic current density  $\mathbf{j}_F(\mathbf{r}_s, t)$  (in  $\text{A m}^{-2}$ ) due to the redox reaction and the intercalation of lithium ions (species 1) is typically described by the

generalized Frumkin-Butler-Volmer model,<sup>23,25,58,59</sup> i.e.,

$$\mathbf{j}_F(\mathbf{r}_s, t) = j_{F,0}(\mathbf{r}_s, t) \left\{ \exp \left[ \frac{(1-\alpha)z_{1,E}F\eta(\mathbf{r}_s, t)}{R_u T} \right] - \exp \left[ \frac{-\alpha z_{1,E}F\eta(\mathbf{r}_s, t)}{R_u T} \right] \right\} \mathbf{n}_s \quad [8]$$

where  $\mathbf{r}_s$  is the position vector for a point on the electrode/electrolyte interface and  $\mathbf{n}_s$  is the unit normal vector to the electrode/electrolyte interface pointing into the electrolyte. Here,  $\alpha$ ,  $\eta(\mathbf{r}_s, t)$ , and  $j_{F,0}(\mathbf{r}_s, t)$  are the transfer coefficient, surface overpotential, and exchange current density, respectively. The surface overpotential  $\eta(\mathbf{r}_s, t) = \Delta\psi_H(\mathbf{r}_s, t) - \Delta\psi_{eq}(\mathbf{r}_s, t)$  (in V) represents the deviation of the electric potential drop across the Stern layer  $\Delta\psi_H$  from its value at equilibrium  $\Delta\psi_{eq}$ .<sup>25</sup> Here,  $\Delta\psi_H$  is defined as the difference between the potential at the pseudocapacitive electrode/electrolyte interface and that at the Stern/diffuse layer interface, i.e.,  $\Delta\psi_H(\mathbf{r}_s, t) = \psi(\mathbf{r}_s, t) - \psi(\mathbf{r}_s + H\mathbf{n}_s, t)$ . The exchange current density  $j_{F,0}$  is expressed as<sup>54,60</sup>

$$j_{F,0}(\mathbf{r}_s, t) = z_{1,E}Fk_0[c_{1,E}(\mathbf{r}_s + H\mathbf{n}_s, t)]^{1-\alpha}[c_{1,P,max} - c_{1,P}(\mathbf{r}_s, t)]^\alpha \times [c_{1,P}(\mathbf{r}_s, t)]^\alpha \quad [9]$$

where  $c_{1,P,max}$  is the theoretical maximum concentration of intercalated  $\text{Li}^+$  in the pseudocapacitive electrode and  $k_0$  is the reaction rate constant in  $\text{m}^{1+3\alpha}\text{mol}^{-\alpha}\text{s}^{-1}$ . For the reaction considered in the present study (Equation 2),  $z_{1,E} = 1$ . Note, however, that Equations 8 and 9 are also applicable to reactions of anions ( $z_{1,E} < 0$ ) or larger-valency cations ( $z_{1,E} > 1$ ). Finally, the transfer coefficient  $\alpha$  was taken as  $\alpha = 1/2$  corresponding to identical energy barriers for the forward and backward redox reactions.<sup>23,25</sup>

The above governing equations were expressed in their general form independent of the coordinate system or a specific cell geometry. The present study of a one-dimensional (1D) hybrid pseudocapacitor (Figure 2b) used 1D Cartesian coordinates with the origin located at the separator centerline. Then, the pseudocapacitive electrode/electrolyte interface was located at  $x = -L$  while the Stern/diffuse layer interface was at  $x = -L + H$ . The pseudocapacitive electrode was located at  $-L - L_P \leq x \leq -L$  and the carbon electrode at  $L \leq x \leq L + L_C$ . The present study will treat all vector variables (e.g.,  $\mathbf{j}_F$ ,  $\mathbf{N}_{i,P}$ ,  $\mathbf{N}_{i,E}$ ) as scalars, positive if they point in the positive  $x$ -direction, and negative if in the negative  $x$ -direction. In addition, because  $j_F$ ,  $j_{F,0}$ ,  $\eta$ , and  $\Delta\psi_H$  were defined only at a single point  $x = -L$ , they will be treated as functions of time only, i.e.,  $j_F(t)$ ,  $j_{F,0}(t)$ ,  $\eta(t)$ , and  $\Delta\psi_H(t)$ . Note that  $\text{Li}^+$  intercalation corresponds to faradaic current density in the negative  $x$ -direction, i.e.,  $j_F < 0 \text{ mA cm}^{-2}$ .

**Initial and boundary conditions.**—The governing Equations 3 to 7 in 1D Cartesian coordinates for  $\psi(x, t)$ ,  $c_{1,P}(x, t)$ , and  $c_{i,E}(x, t)$  are first-order partial differential equations in time and second order in space. Thus, each equation requires one initial condition and two boundary conditions in each region where it is solved.

**Initial conditions.**—Initially, the potential was taken as uniform and equal to zero across the device such that

$$\psi(x, 0) = 0 \text{ V.} \quad [10]$$

The initial ion concentrations in the diffuse layer ( $-L + H \leq x \leq L - H$ ) were uniform with bulk concentrations  $c_{i,E,\infty}$  satisfying electroneutrality so that

$$c_{i,E}(x, 0) = c_{i,E,\infty} \quad \text{with} \quad \sum_{i=1}^2 z_{i,E}c_{i,E,\infty} = 0 \quad [11]$$

The initial concentration of  $\text{Li}^+$  intercalated in the pseudocapacitive electrode ( $-L - L_P \leq x \leq -L$ ) was uniform and equal to  $c_{1,P,0}$ , i.e.,

$$c_{1,P}(x, 0) = c_{1,P,0} \quad [12]$$

Note that an initial concentration  $c_{1,P,0}$  of identically zero resulted in zero faradaic current density  $j_F$  (Equation 8) at all subsequent times. Thus, initially “empty” electrodes charged by intercalation were simulated using an arbitrary small, but non-zero, value of the initial  $\text{Li}^+$  concentration  $c_{1,P,0}$ . It was verified that the predictions for  $\psi(x, t)$ ,  $c_{1,P}(x, t)$ , and  $c_{i,E}(x, t)$  under oscillatory steady state were not sensitive to the choice of  $c_{1,P,0}$ .

**Boundary conditions.**—Under galvanostatic cycling, the current density  $j_{im}(t) = \pm j_s$  was imposed at the interface between the current collector and the pseudocapacitive electrode located at  $x = -L - L_P$  according to Ohm’s law and expressed as<sup>25</sup>

$$-\sigma_P \frac{\partial \psi}{\partial x}(-L - L_P, t) = j_{im}(t). \quad [13]$$

In the present study, the amount of charge  $\Delta q_s = j_s t_c/2$  stored during the charging step and retrieved during the discharging step was kept identical for all cycles and charging corresponded to  $\text{Li}^+$  intercalation. The imposed current density  $j_{im}(t)$  alternated between charging and discharging as a square wave of fixed cycle period  $t_c$  expressed as

$$j_{im}(t) = \begin{cases} -j_s & \text{for charging } (n_c - 1)t_c \leq t < (n_c - 1/2)t_c \\ j_s & \text{for discharging } (n_c - 1/2)t_c \leq t < n_c t_c \end{cases} \quad [14]$$

where  $n_c = 1, 2, 3, \dots$  is the cycle number. Note that ECs are often experimentally cycled over a fixed potential window  $\Delta\psi_s$  rather than with fixed  $\Delta q_s$ . The fixed-charge method was used here to facilitate the physical interpretation and the comparison with previous EDLC simulations.<sup>61,62</sup>

Charge conservation required the electronic current density in the pseudocapacitive electrode at the electrode/electrolyte interface to equal the sum of the faradaic current density  $j_F(t)$ , given by Equation 8, and the capacitive current density  $j_C(t)$  at the Stern/diffuse layer interface such that

$$-\sigma_P \frac{\partial \psi}{\partial x}(-L, t) = j_F(t) + j_C(t). \quad [15]$$

The capacitive current density  $j_C(t)$  arises due to the formation and dissolution of the EDL near the pseudocapacitive electrode. It is defined as the displacement current density within the Stern layer at the pseudocapacitive electrode. It was uniform across the Stern layer due to the uniform potential gradient and given by

$$j_C(t) = -\epsilon_0 \epsilon_r \frac{\partial^2 \psi}{\partial x \partial t}(-L + H, t). \quad [16]$$

The electric potential gradient was uniform across the Stern layers near each electrode due to the lack of free charge (Equation 5). The potential  $\psi(x, t)$  in the Stern layers was not explicitly simulated. Instead, it was accounted for by the boundary conditions.<sup>35,63</sup> At the Stern/diffuse layer interface near the pseudocapacitive electrode, it was expressed as<sup>33,52</sup>

$$\frac{\partial \psi}{\partial x}(-L + H, t) = \frac{\psi(-L + H, t) - \psi(-L, t)}{H}. \quad [17]$$

Similarly, at the Stern/diffuse layer interface near the carbon electrode, the potential satisfied

$$\frac{\partial \psi}{\partial x}(L - H, t) = \frac{\psi(L, t) - \psi(L - H, t)}{H}. \quad [18]$$

At the carbon electrode/electrolyte interface, located at  $x = L$ , the electronic current density equaled the displacement current density at the Stern/diffuse layer interface such that

$$-\sigma_C \frac{\partial \psi}{\partial x}(L, t) = -\epsilon_0 \epsilon_r \frac{\partial^2 \psi}{\partial x \partial t}(L - H, t). \quad [19]$$

Finally, the interface between the carbon electrode and the current collector was electrically grounded such that

$$\psi(L + L_C, t) = 0 \text{ V.} \quad [20]$$

Note that the choice of reference potential is arbitrary. It did not affect the computed currents, ion concentrations, or cell potential  $\psi_s(t)$ .

Moreover, lithium ions could not intercalate into the current collector so that

$$N_{1,P}(-L - L_P, t) = 0 \text{ mol m}^{-2}\text{s}^{-1}. \quad [21]$$

The molar fluxes of  $\text{Li}^+$  in the electrolyte and intercalated  $\text{Li}^+$  entering and exiting the Stern layer near the pseudocapacitive electrode were proportional to the faradaic current density  $j_F(t)$  (Equation 8), while the anion mass flux vanished so that

$$N_{1,P}(-L, t) = N_{1,E}(-L + H, t) = \frac{j_F(t)}{z_{1,E}F} \quad \text{and} \quad [22]$$

$$N_{2,E}(-L + H, t) = 0 \text{ mol m}^{-2}\text{s}^{-1}.$$

In addition, both ion mass fluxes vanished at the Stern/diffuse layer interface near the carbon electrode as no ion intercalation occurred, i.e.,

$$N_{i,E}(L - H, t) = 0 \text{ mol m}^{-2}\text{s}^{-1} \quad \text{for } i = 1 \text{ and } 2. \quad [23]$$

**Constitutive relationships.**— The present study uses arbitrary yet realistic material properties for the pseudocapacitive material. Its electrical conductivity  $\sigma_P$  was taken as  $\sigma_P = 7 \times 10^{-2} \text{ S m}^{-1}$ , within the range typical of metal oxides used in pseudocapacitors.<sup>64</sup> As previously mentioned, the transfer coefficient was taken as  $\alpha = 1/2$  corresponding to identical energy barriers for the reaction in both directions. For transition metal oxides, the reaction rate coefficient  $k_0$  for  $\text{Li}^+$  intercalation typically ranged from about  $10^{-11}$  to  $10^{-8} \text{ m}^{5/2}\text{mol}^{-1/2}\text{s}^{-1}$ <sup>60,65–67</sup> and the diffusion coefficient  $D_{1,P}$  from  $10^{-18}$  to  $10^{-10} \text{ m}^2\text{s}^{-1}$ .<sup>66,68</sup> Here, they were taken as  $k_0 = 5 \times 10^{-9} \text{ m}^{5/2}\text{mol}^{-1/2}\text{s}^{-1}$  and  $D_{1,P} = 10^{-10} \text{ m}^2\text{s}^{-1}$  to provide favorable conditions for faradaic charge storage. The maximum concentration of intercalated  $\text{Li}^+$  in the pseudocapacitive electrode was approximated as  $c_{1,P,\text{max}} = 2\rho_P/M_P \approx 32.9 \text{ mol L}^{-1}$  where  $M_P = 279.7 \text{ g mol}^{-1}$  and  $\rho_P \approx 4.6 \text{ g cm}^{-3}$  correspond to the molecular mass and density of fully-intercalated  $\text{Li}_2\text{Nb}_2\text{O}_5$ , respectively. The initial  $\text{Li}^+$  concentration in the electrode was  $c_{1,P,0} = 10^{-6} \text{ mol L}^{-1}$ . Finally, the electrical conductivity of the simulated carbon electrode was taken as  $\sigma_C = 100 \text{ S m}^{-1}$ .<sup>69–71</sup>

Experimental studies<sup>31,72</sup> have shown that the equilibrium potential drop  $\Delta\psi_{eq}$  for pseudocapacitive electrodes may vary with the state of charge and thus change over time during operation. Ref. 31 expressed  $\Delta\psi_{eq}$  of  $\text{MnO}_2$  as a linear function of the oxidation state of the pseudocapacitive material according to

$$\Delta\psi_{eq} = A \left( Os_{\text{max}} - \frac{c_{1,P}}{c_{1,P,\text{max}}} \right) + B \quad [24]$$

where  $Os_{\text{max}} = 4$  was the theoretical maximum oxidation state for  $\text{MnO}_2$  and  $A$  and  $B$  were empirically fitted constants expressed in V. The present study expresses  $\Delta\psi_{eq}$  in slightly different form, i.e.,

$$\Delta\psi_{eq}(t) = \Delta\psi_{eq,0} - S_{eq} \left( \frac{c_{1,P}(-L, t) - c_{1,P,0}}{c_{1,P,\text{max}}} \right). \quad [25]$$

where  $\Delta\psi_{eq,0}$  is the initial value of  $\Delta\psi_{eq}$  corresponding to  $c_{1,P}(-L, t) = c_{1,P,0}$ . Equations 24 and 25 are equivalent with  $S_{eq} = A$  and  $\Delta\psi_{eq,0} = B + A(Os_{\text{max}} - c_{1,P,0}/c_{1,P,\text{max}})$ . The present study assumed that the cell started from an equilibrium state such that  $\Delta\psi_{eq,0} = 0 \text{ V}$ , consistent with Equation 10. Note that  $\Delta\psi_{eq,0} \neq 0 \text{ V}$  could be simulated with appropriate initial conditions, e.g., non-uniform electric potential and ion concentrations corresponding an equilibrium state such that  $\Delta\psi_H(0) = \Delta\psi_{eq,0}$ , but this is beyond the scope of the present investigation. Here, we primarily considered the ideal faradaic behavior  $S_{eq} = 0 \text{ V}$  when  $\Delta\psi_{eq}$  is constant. The effects of variable  $\Delta\psi_{eq}$  were investigated using  $S_{eq} = 1 \text{ V}$  and  $S_{eq} = 10.5 \text{ V}$  based on experimentally measured values for thin-film and thick porous  $\text{MnO}_2$  electrodes, respectively.<sup>31</sup> Equation 25 indicates that, for  $S_{eq} > 0 \text{ V}$  as measured experimentally for  $\text{MnO}_2$ ,  $\Delta\psi_{eq}$  decreases with increasing  $c_{1,P}$ . This makes intuitive sense, since it results in further cation intercalation becoming increasingly “difficult” with increasing  $c_{1,P}$  (i.e., the potential drop  $\Delta\psi_H$  must be more

negative to achieve the same  $\eta_F < 0 \text{ V}$  than for smaller  $c_{1,P}$ ) while deintercalation becomes “easier” (i.e.,  $\eta_F > 0 \text{ V}$  can be achieved with smaller  $\Delta\psi_H$ ).

The binary and asymmetric electrolyte simulated corresponded to  $1 \text{ mol L}^{-1} \text{ LiClO}_4$  in propylene carbonate (PC) solvent. The relative permittivity  $\epsilon_r = 66.1$  was taken as constant and equal to that of PC at zero electric field.<sup>73</sup> The solvated ion diameters of  $\text{Li}^+$  and  $\text{ClO}_4^-$  were taken as  $a_{1,E} = 0.67 \text{ nm}$  and  $a_{2,E} = 1.0 \text{ nm}$ , respectively.<sup>73,74</sup> Their diffusion coefficients in PC were  $D_{1,E} = 2.6 \times 10^{-10} \text{ m}^2\text{s}^{-1}$  and  $D_{2,E} = 3.3 \times 10^{-10} \text{ m}^2\text{s}^{-1}$ , respectively.<sup>74,75</sup> Their bulk concentrations equaled  $c_{1,E,\infty} = c_{2,E,\infty} = 1 \text{ mol L}^{-1}$ .

The pseudocapacitive and carbon electrodes had the same thickness  $L_P = L_C = 5 \text{ nm}$  while the inter-electrode half-width was much larger and equal to  $L = 1 \text{ }\mu\text{m}$ . The use of thin electrodes facilitated comparison to analytical calculations in the limiting case when the intercalated  $\text{Li}^+$  concentration  $c_{1,P}(x, t)$  remained uniform in the pseudocapacitive electrode. The temperature was taken as uniform, constant, and equal to  $T = 298 \text{ K}$ . The cell was cycled galvanostatically at various current densities  $j_s$  and cycle periods  $t_c$  such that the stored charge density  $\Delta q_s = j_s t_c / 2 = 0.3 \text{ C m}^{-2}$  added to the cell during charging and removed during discharging was the same for all cases. This charge density was comparable to the charge density per unit electrode/electrolyte interfacial area for experimentally cycled EDLCs and hybrid pseudocapacitors reported in the literature.<sup>76,77</sup>

**Method of solution.**— The 1D governing Equations 3 to 7 and the associated initial and boundary conditions were solved numerically using finite element methods. Numerical convergence was assessed based on the predicted potential  $\psi(x, t)$  and concentrations  $c_{1,E}(x, t)$ ,  $c_{2,E}(x, t)$ , and  $c_{1,P}(x, t)$ . The mesh element size was the smallest at the Stern/diffuse layer interfaces due to the large potential and concentration gradients in this region and gradually increased away from these boundaries. The mesh was refined by reducing the element size at the Stern/diffuse layer interface and by reducing the maximum element growth rate. The time step was controlled by the relative and absolute time tolerances.<sup>78</sup> The numerical solution was considered converged when halving (i) the element size at the Stern/diffuse layer interface, (ii) the maximum element growth rate, and (iii) both the relative and absolute tolerances resulted in less than 0.5% maximum relative difference in  $\psi$ ,  $c_{1,E}$ ,  $c_{2,E}$ , and  $c_{1,P}$ . At each time step, the estimated local error between the solutions at the previous and the current time steps was compared with the time tolerances. The time step was then adjusted until the convergence criterion was satisfied, as described in Ref. 78. This enabled the use of small time steps during periods when the different variables of interest changed rapidly while using a larger time step for the rest of the simulation.

Finally, several cycles were simulated and an oscillatory steady state in  $\psi(x, t)$ ,  $c_{1,E}(x, t)$ ,  $c_{2,E}(x, t)$ , and  $c_{1,P}(x, t)$  was considered to be reached when the maximum relative error between the value of each variable at time  $t$  and its value at time  $t - t_c$  was less than 1%. For small current densities  $j_s \lesssim 8 \text{ mA cm}^{-2}$ , these conditions were typically met by the third cycle. The number of cycles required to reach oscillatory steady state increased with increasing current density  $j_s$ . For example, at current density  $j_s = 256 \text{ mA cm}^{-2}$ , almost 80 cycles were required to reach oscillatory steady state.

**Analytical expressions for limiting cases.**— The preceding model accounts simultaneously for two contributions to charge storage: (i) faradaic charge storage associated with the faradaic current density  $j_F(t)$  and (ii) EDL charge storage associated with the capacitive current density  $j_C(t)$ . The complex interactions between the faradaic reaction and the EDL formation can make physical interpretation of the model predictions difficult. The latter can be facilitated by simpler analytical expressions for certain variables such as  $c_{1,P}$  and  $\eta$  as functions of time derived in the limiting cases when one of the storage mechanisms dominates. This section analyzes these two limiting cases in more detail. Here, the intercalated  $\text{Li}^+$  concentration  $c_{1,P}$  was assumed to be uniform in the pseudocapacitive electrode due to its

small thickness. Note that the expressions derived for  $c_{1,P}$  and  $\eta$  are valid for charging either by intercalation or by deintercalation.

**General expressions.**—First, it is useful to express the intercalated  $\text{Li}^+$  concentration  $c_{1,P}$  and the overpotential  $\eta$  as functions of the current densities  $j_F$  and  $j_C$ . Based on mass conservation, the uniform intercalated  $\text{Li}^+$  concentration  $c_{1,P}(x, t)$  at time  $t$  is the sum of the initial concentration  $c_{1,P,0}$  and the net  $\text{Li}^+$  intercalated due to the faradaic reaction per unit volume of the electrode, i.e.,

$$c_{1,P}(x, t) = c_{1,P,0} + \frac{A_P}{z_{1,E}F} \int_0^t [-j_F(t)] dt. \quad [26]$$

Here,  $A_P$  is the pseudocapacitive electrode/electrolyte interfacial area per unit volume of pseudocapacitive material (in  $\text{m}^{-1}$ ). It is given by  $A_P = 1/L_P$  for a 1D cell with planar electrodes. The second term is positive and  $c_{1,P}$  increases during  $\text{Li}^+$  intercalation corresponding to negative  $j_F(t)$ , as previously mentioned.

Moreover, for  $\alpha = 1/2$ , the expression of  $j_F(t)$  given by Equations 8 and 9 can be solved for  $\eta(t)$  to yield

$$\eta(t) = 2 \frac{R_u T}{z_{1,E} F} \sinh^{-1} \left( \frac{j_F(t)}{2 z_{1,E} F k_0 \sqrt{c_{1,E}(-L + H, t)} \sqrt{c_{1,P, \max} - c_{1,P}(-L, t)} \sqrt{c_{1,P}(-L, t)}} \right). \quad [27]$$

Alternatively,  $\eta(t)$  can be expressed in terms of the EDL surface charge density  $q_{s,C}(t)$  stored in the EDL at the pseudocapacitive electrode and of the Stern layer capacitance  $C_s^{St} = \epsilon_0 \epsilon_r / H$  as<sup>52</sup>

$$\begin{aligned} \eta(t) &= \Delta\psi_H(t) - \Delta\psi_{eq}(t) = \frac{q_{s,C}(t)}{C_s^{St}} - \Delta\psi_{eq}(t) \\ &= \frac{H q_{s,C}(t)}{\epsilon_0 \epsilon_r} - \Delta\psi_{eq}(t). \end{aligned} \quad [28]$$

The EDL surface charge density  $q_{s,C}(t)$  at the pseudocapacitive electrode is equal to  $q_{s,C}(t) = \int_0^t j_C(t') dt'$ . Thus, the time rate of change of  $\eta$  varies linearly with the capacitive current density  $j_C(t) = dq_{s,C}/dt$  according to

$$\frac{d\eta}{dt}(t) = \frac{j_C(t)H}{\epsilon_0 \epsilon_r} - \frac{d\Delta\psi_{eq}(t)}{dt}. \quad [29]$$

**Asymptotic faradaic regime.**—In the faradaic regime, the faradaic current density  $j_F(t)$  carries most of the imposed current density  $j_s$  so that  $j_F(t) \approx \pm j_s$  and  $j_C(t) \approx 0$   $\text{mA cm}^{-2}$ . Then, based on Equation 26, the corresponding  $\text{Li}^+$  concentration  $c_{1,P,F}(x, t)$  varies linearly as a function of  $t$  with slope  $j_s A_P / z_{1,E} F$  and can be expressed as

$$c_{1,P,F}(t) = c_{1,P,0} + (-1)^p \begin{cases} \frac{j_s t_c A_P}{z_{1,E} F} \left( \frac{t}{t_c} - n_c + 1 \right) & \text{for charging} \\ \frac{j_s t_c A_P}{z_{1,E} F} \left( n_c - \frac{t}{t_c} \right) & \text{for discharging} \end{cases} \quad [30]$$

where  $p = 0$  for charging by  $\text{Li}^+$  intercalation (analogous to  $\text{Nb}_2\text{O}_5$  negative electrodes) and  $p = 1$  for charging by  $\text{Li}^+$  deintercalation (analogous to  $\text{MnO}_2$  positive electrodes). In the faradaic regime, EDL formation near the pseudocapacitive electrode is expected to be negligible, and the ion concentrations at the Stern/diffuse layer interface to remain close to their bulk concentrations such that  $c_{1,E}(-L + H, t) \approx c_{1,E,\infty}$  and  $c_{2,E}(-L + H, t) \approx c_{2,E,\infty}$ . Then, Equation 27 for the surface overpotential  $\eta_F(t)$

simplifies as

$$\eta_F(t) = \frac{2 R_u T}{z_{1,E} F} \sinh^{-1} \left[ \frac{j_{im}(t)/2 z_{1,E} F k_0}{\sqrt{c_{1,E,\infty}} \sqrt{c_{1,P,\max} - c_{1,P,F}(t)} \sqrt{c_{1,P,F}(t)}} \right]. \quad [31]$$

Here, the overpotential magnitude  $|\eta_F|$  required to drive the current density  $j_F(t) = \pm j_s$  and predicted by Equation 31 decreases with decreasing  $j_s$ , increasing reaction rate constant  $k_0$ , increasing  $c_{1,E,\infty}$ , and/or  $c_{1,P,F}$  approaching  $c_{1,P,\max}/2$ .

**Asymptotic capacitive regime.**—We define the capacitive regime as the limiting case in which the capacitive current density  $j_C(t)$  carries the entire imposed current density  $j_{im}(t)$  such that  $j_C(t) \approx \pm j_s$  while the faradaic current density is negligible, i.e.,  $j_F(t) \approx 0$   $\text{mA cm}^{-2}$ . Then, the  $\text{Li}^+$  concentration inside the pseudocapacitive electrode and thus  $\Delta\psi_{eq}$  (Equation 25) are approximately constant, i.e.,  $c_{1,P}(x, t) \approx c_{1,P,C}$  and  $\Delta\psi_{eq} \approx \Delta\psi_{eq,C}$ . Note that the steady-state concentration  $c_{1,P,C}$  could differ significantly from the initial value  $c_{1,P,0}$  despite the small magnitude of  $j_F(t)$  when the number of cycles required to reach oscillatory steady state is large. Then, according to Equation 29, the

overpotential  $\eta_C(t)$  varies linearly with time such that

$$\frac{d\eta_C}{dt}(t) = \frac{j_{im}(t)H}{\epsilon_0 \epsilon_r} = \pm \frac{j_s H}{\epsilon_0 \epsilon_r}. \quad [32]$$

The value of  $\eta_C$  at the beginning of the cycle depends on the EDL charge density  $q_{s,C}(n_c t_c - t_c)$ . For cycling with fixed  $\Delta q_s$ , the total stored charge density from the external circuit  $q_s(t) = q_{s,C}(t) + q_{s,F}(t)$  is zero at the beginning of the cycle, so the EDL charge density is given by  $q_{s,C}(n_c t_c - t_c) = -q_{s,F}(n_c t_c - t_c) = z_{1,E} F (c_{1,P,C} - c_{1,P,0}) / A_P$  and

$$\eta_C(n_c t_c - t_c) = \frac{H}{\epsilon_0 \epsilon_r} \frac{z_{1,E} F (c_{1,P,C} - c_{1,P,0})}{A_P} - \Delta\psi_{eq,C}. \quad [33]$$

Note that for EDLCs with no faradaic reactions,<sup>61,62</sup>  $c_{1,P,C} = c_{1,P,0}$  and  $\eta(t)$  returned to 0 V at the end of each cycle.

## Results and Discussion

This section presents simulation results for the previously described hybrid pseudocapacitor charged by  $\text{Li}^+$  intercalation, analogous to  $\text{Nb}_2\text{O}_5$  as a negative electrode. Various current densities  $j_s$  and cycle periods  $t_c$  were explored for the same amount of stored charge  $\Delta q_s = j_s t_c / 2 = 0.3$   $\text{C m}^{-2}$ . First, detailed results are presented for constant equilibrium potential drop  $\Delta\psi_{eq}$ . Then, the effect of state-of-charge-dependent  $\Delta\psi_{eq}$  are briefly illustrated. Finally, results for a hybrid cell charged by  $\text{Li}^+$  deintercalation with constant equilibrium potential drop  $\Delta\psi_{eq}$  are presented.

**Current densities.**— Figures 3a and 3b respectively show the numerically predicted faradaic current density  $j_F(t)$  (Equation 8) and capacitive current density  $j_C(t)$  (Equation 16) as functions of dimensionless time  $t/t_c$  for various pairs of  $[j_s, t_c]$  under galvanostatic cycling at oscillatory steady state. For small values of  $j_s$  ( $< 4$   $\text{mA cm}^{-2}$ ), the faradaic current density  $j_F(t)$  was negative during charging, positive during discharging, and constant in magnitude during most of the cycle. The capacitive current density  $j_C(t)$  was small compared to  $j_F(t)$ . On the other hand, for large values of  $j_s$  ( $> 32$   $\text{mA cm}^{-2}$ ), the capacitive current density  $j_C(t)$  was significantly larger than  $j_F(t)$  at all times. In fact, the maximum value of  $|j_C|$  increased

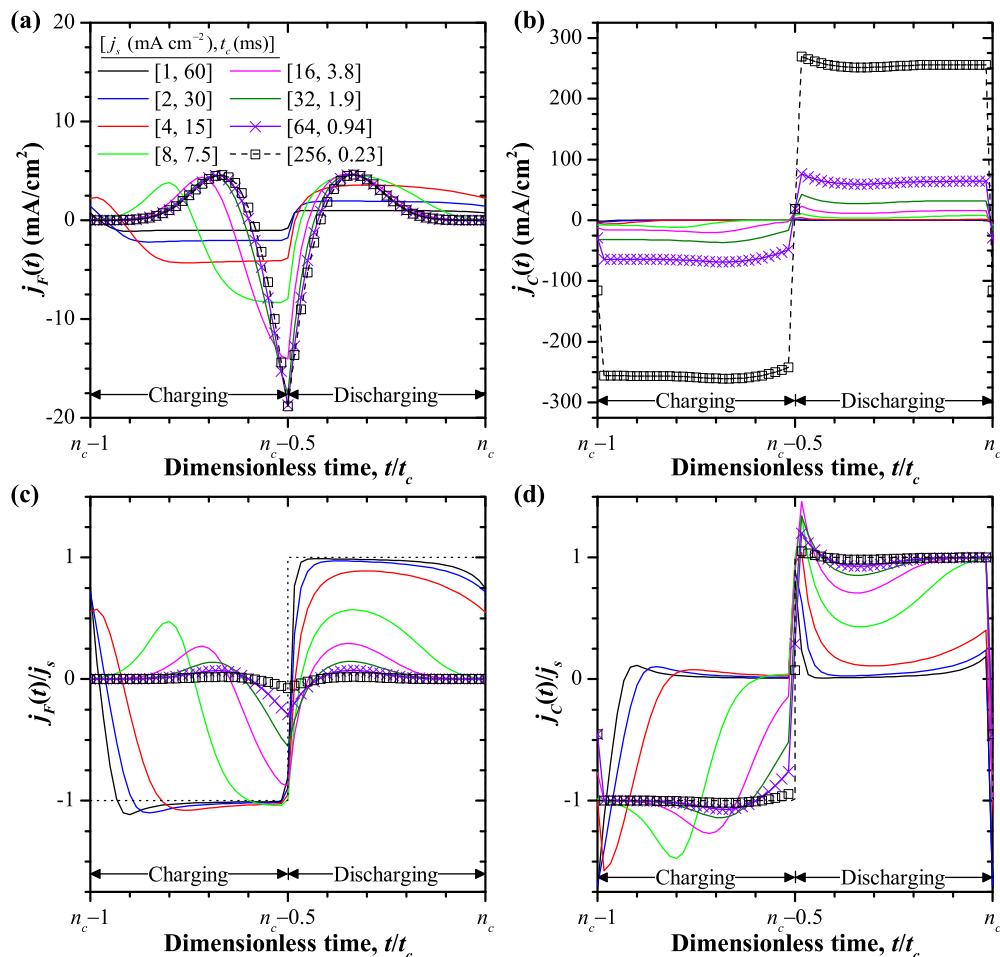


**Figure 3.** Predicted (a) faradaic current density  $j_F(t)$  and (b) capacitive current density  $j_C(t)$  as well as the faradaic and capacitive fractions (c)  $j_F(t)/j_s$  and (d)  $j_C(t)/j_s$  of the total current density as functions of dimensionless time  $t/t_c$  for different values of  $j_s$  and  $t_c$  under galvanostatic cycling and oscillatory steady state. Here,  $j_s$  and  $t_c$  were chosen such that  $\Delta q_s = j_s t_c / 2 = 0.3 \text{ C m}^{-2}$ .

continuously with increasing  $j_s$ . By contrast, the faradaic current density  $j_F(t)$  approached an asymptotic limit at large  $j_s$ .

Figures 3c and 3d respectively show the fractions of the imposed current density  $j_F(t)/j_s$  carried by the faradaic current and  $j_C(t)/j_s$  carried by the capacitive current as functions of dimensionless time  $t/t_c$  for various values of  $j_s$  and  $t_c$  under galvanostatic cycling. For small values of  $j_s$ , the current density was almost exclusively faradaic, i.e.,  $j_F(t) \gg j_C(t)$  and  $j_F(t)/j_s \approx \pm 1$ . Then,  $j_F(t)$  diverged from the imposed current density  $j_{im}(t) = \pm j_s$  only around the charging/discharging transitions at  $t/t_c = n_c - 1$  and  $t/t_c = n_c - 0.5$ . Simultaneously, the capacitive current fraction  $j_C(t)/j_s$  featured peaks following these transitions so that the sum  $j_F(t) + j_C(t)$  always equaled  $j_{im}(t) = \pm j_s$ . The faradaic contribution  $j_F(t)/j_s$  decreased with increasing  $j_s$ . Indeed, for  $j_s = 256 \text{ mA cm}^{-2}$ , the current density was almost entirely capacitive, i.e.,  $j_C(t) \gg j_F(t)$  at all times and  $j_C(t)/j_s \approx \pm 1$ .

Overall, two asymptotic regimes were evident: a faradaic regime characterized by  $j_F(t) \approx j_{im}(t)$  for small values of  $j_s$  and slow cycling and a capacitive regime featuring  $j_C(t) \approx j_{im}(t)$  for large values of  $j_s$  and fast cycling.

*Intercalated  $\text{Li}^+$  concentration in the pseudocapacitive electrode.*— Figure 4 shows the predicted concentration of intercalated  $\text{Li}^+$   $c_{1,p}(-L, t)$  at the pseudocapacitive electrode/electrolyte interface as a function of dimensionless time  $t/t_c$  for different values

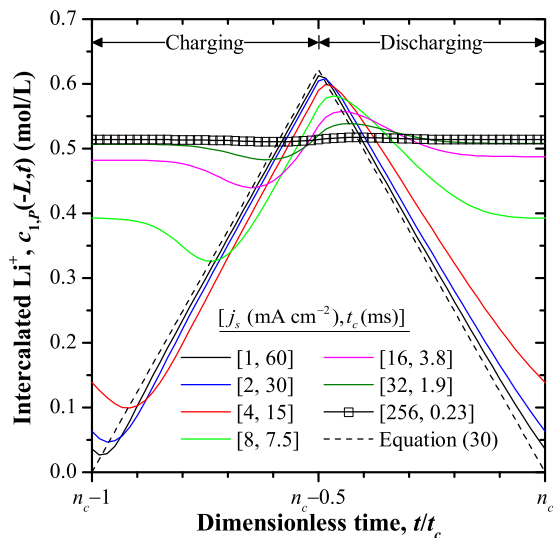


**Figure 4.** Predicted concentration  $c_{1,p}(-L, t)$  of intercalated  $\text{Li}^+$  in the pseudocapacitive electrode as a function of dimensionless time  $t/t_c$  over one cycle at oscillatory steady state for different values of  $j_s$  and  $t_c$  such that  $\Delta q_s = j_s t_c / 2 = 0.3 \text{ C m}^{-2}$ . The concentration was uniform throughout the pseudocapacitive electrode.



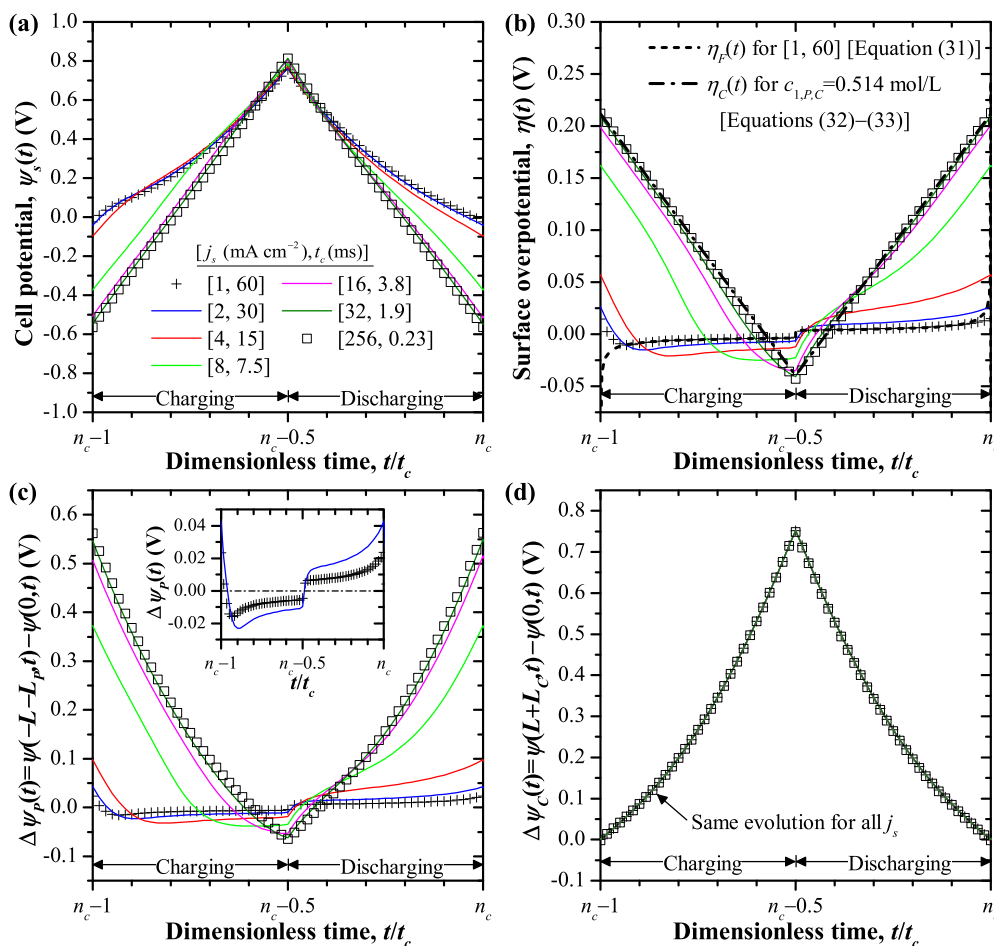


**Figure 5.** Predicted (a) cell potential  $\psi_s(t) = \Delta\psi_C(t) - \Delta\psi_P(t) = \psi(L + L_C, t) - \psi(-L - L_P, t)$  and (b) pseudocapacitive electrode surface overpotential  $\eta(t)$  as well as the potential drops (c)  $\Delta\psi_P(t) = \psi(-L - L_P, t) - \psi(0, t)$  between the pseudocapacitive electrode and the bulk electrolyte and (d)  $\Delta\psi_C(t) = \psi(L + L_C, t) - \psi(0, t)$  between the carbon electrode and the bulk electrolyte as functions of dimensionless time  $t/t_c$  over one cycle during galvanostatic cycling for various values of  $j_s$  and  $t_c$  such that  $\Delta q_s = j_s t_c / 2 = 0.3 \text{ C m}^{-2}$ .

of  $j_s$  and  $t_c$  under galvanostatic cycling. In all cases,  $c_{1,P}$  was uniform throughout the electrode due to the small electrode thickness  $L_P = 5 \text{ nm}$  and to the relatively large diffusion coefficient  $D_{1,P}$ . In fact, the penetration depth, defined as  $d_p = \sqrt{D_{1,P} t_c}$ , ranged from 150 nm to 2400 nm as the cycle period ranged from 0.23 ms to 60 ms. Thus,  $d_p$  was much larger than the electrode thickness  $L_P$  of 5 nm. In other words,  $\text{Li}^+$  diffusion in the electrode was fast and never limiting.

In the faradaic regime,  $c_{1,P}$  increased almost linearly during the charging step and decreased linearly during the discharging step. Indeed, for  $j_s = 1 \text{ mA cm}^{-2}$ , the numerically predicted  $\text{Li}^+$  concentration  $c_{1,P}(-L, t)$  agreed very well with that predicted by Equation 30, derived from mass conservation considerations and assuming  $j_F(t) = \pm j_s$ . The largest discrepancies occurred near the transition from discharging to charging, when  $c_{1,P}$  was small and  $j_F(t)$  differed from  $\pm j_s$  (Figure 3). In the capacitive regime,  $c_{1,P}$  remained approximately constant and equal to  $c_{1,P,C} \approx 0.514 \text{ mol L}^{-1}$ .

**Electric potentials.**— Figure 5 shows (a) the cell potential  $\psi_s(t) = \Delta\psi_C(t) - \Delta\psi_P(t) = \psi(L + L_C, t) - \psi(-L - L_P, t)$ , (b) the surface overpotential  $\eta(t)$ , and the potential drop between the electrode/current collector interface and the electrolyte centerline (c)  $\Delta\psi_P(t) = \psi(-L - L_P, t) - \psi(0, t)$  for the pseudocapacitive electrode half-cell and (d)  $\Delta\psi_C(t) = \psi(L + L_C, t) - \psi(0, t)$  for the carbon electrode half-cell as functions of dimensionless time  $t/t_c$  for different current densities  $j_s$  and cycle periods  $t_c$  for galvanostatic cycling at oscillatory steady state. Here,  $\Delta\psi_P(t)$  and  $\Delta\psi_C(t)$  are equivalent to

the electrode potentials measured relative to a reference electrode in three-electrode measurements (plus or minus a constant), since reference electrodes are designed to have constant potential relative to the electrolyte solution.<sup>23,25</sup>

Figure 5a indicates that  $\psi_s(t)$  increased throughout the charging step and decreased during the discharging step for all cases considered. The potential window  $\Delta\psi_s = \psi_{\max} - \psi_{\min}$  increased with increasing  $j_s$ , corresponding to decreasing integral capacitance  $C_{s,int}$  (Equation 1) as the faradaic fraction of the charge storage decreased. In the faradaic regime, corresponding to small current density  $j_s$ , the cell potential  $\psi_s$  returned to  $\psi_{\max} \approx 0 \text{ V}$  at the beginning and end of the cycle when fully discharged. The temporal evolution of  $\psi_s$  was asymmetric around the transition from charging to discharging at  $t/t_c = n_c - 0.5$ . At the beginning of the charging step, the time rate of change  $|d\psi_s/dt|$  was relatively large for a short period. After this brief period,  $|d\psi_s/dt|$  sharply decreased, resulting in a distinct “kink” in the  $\psi_s(t)$  curve. In fact, it qualitatively resembled that measured experimentally (Figure 1a).<sup>9,12,14,21</sup> This kink can be attributed to the brief peak of capacitive current  $j_C$  at the beginning of the charging step (Figure 3d) and associated with relatively small differential capacitance  $C_{s,diff}$  and large  $|d\psi_s/dt|$  (Equation 1). Then,  $C_{s,diff}$  abruptly increased and  $|d\psi_s/dt|$  decreased as the faradaic current  $j_F$  became dominant (Figure 3c). In the capacitive regime, under large current density  $j_s$ , the temporal evolution of  $\psi_s$  was linear and symmetric around  $t/t_c = n_c - 0.5$ . The cell changed polarity during each cycle, and  $\psi_s$  was equal to  $\psi_{\min} \approx -0.55 \text{ V}$  at the beginning and end of the cycle. This non-zero cell potential for the fully discharged cell

occurred because a significant amount of  $\text{Li}^+$  originally from the electrolyte remained intercalated as  $\text{Li}^+$  in the electrode, as evidenced by  $c_{1,P,C}$  being significantly larger than the initial concentration  $c_{1,P,0}$ , i.e.,  $c_{1,P,C} - c_{1,P,0} \approx c_{1,P,C} = 0.514 \text{ mol L}^{-1}$  (Figure 4). Then, the electrolyte retained a net negative charge, because more  $\text{ClO}_4^-$  than  $\text{Li}^+$  ions remained in the electrolyte, while the pseudocapacitive electrode had a net positive charge of equal magnitude.

Figure 5b shows that the sign of the surface overpotential  $\eta(t)$  was always the same as that of the faradaic current density  $j_F(t)$ , as suggested by Equations 8 and 27. The magnitude of  $\eta$  increased with increasing  $j_s$ . In the faradaic regime, the magnitude of  $\eta(t)$  was small and varied relatively little with time. For  $j_s = 1 \text{ mA cm}^{-2}$ , the numerical predictions of  $\eta(t)$  agreed very well with  $\eta_F(t)$  predicted analytically by Equation 31 over most of the cycle. The numerical and analytical predictions differed from one another immediately after each charging/discharging transition and at the very end of the cycle. Then,  $\eta_F(t)$  increased rapidly and  $j_C(t)$  was significant, as suggested by Equation 29. Equation 31 indicates that the overpotential  $\eta_F(t)$  required to drive faradaic current density  $j_F(t) = j_{im}(t)$  changed instantaneously when  $j_{im}(t)$  changed sign at the transitions between charging and discharging steps. However, the actual time rate of change of  $\eta(t)$  was finite and related to  $j_C(t) = j_{im}(t) - j_F(t)$  by Equation 29. Thus, the capacitive current density  $j_C(t)$  dominated immediately after charging/discharging transitions until the overpotential approached  $\eta_F(t)$ , as observed in Figure 3. Similarly,  $\eta_F(t)$  increased rapidly and  $j_C$  was significant at the end of the cycle as  $c_{1,P,F}$  approached zero. In the capacitive regime,  $\eta(t)$  varied linearly with  $t/t_c$  with slope  $\pm j_s t_c H / \epsilon_0 \epsilon_r$ . Indeed, for  $j_s = 256 \text{ mA cm}^{-2}$ ,  $\eta(t)$  showed excellent agreement with  $\eta_C(t)$  predicted analytically by Equations 32 and 33 with  $c_{1,P,C} - c_{1,P,0} \approx c_{1,P,C} = 0.514 \text{ mol L}^{-1}$  (Figure 4). Attempts were made to derive an analytical expression for  $\eta(t)$  for intermediate values of  $j_s$ , but were unsuccessful.

Figure 5c indicates that, for the pseudocapacitive electrode, the evolution of  $\Delta\psi_P(t)$  qualitatively resembled that of the surface overpotential  $\eta(t)$  (Figure 5b). In the faradaic regime, it was small, asymmetric around the transition from charging to discharging, and varied relatively little in magnitude over most of the cycle (see inset). As previously mentioned, such a constant potential drop during charging or discharging is characteristic of batteries.<sup>3</sup> Like  $\eta(t)$  and the experimentally measured  $\Delta\psi_P(t)$  (Figure 1a),<sup>12</sup> the potential drop  $\Delta\psi_P(t)$  featured relatively steep slopes  $|d\Delta\psi_P/dt|$  immediately following each charging/discharging transition and near the end of the cycle. However, the experimental  $\Delta\psi_P(t)$  featured significant slope  $|d\Delta\psi_P/dt|$  throughout the cycle, while the numerical  $\Delta\psi_P(t)$  was almost constant when  $j_F$  dominated. This difference may result from SOC-dependence of  $\Delta\psi_{eq}$  which was neglected in the simulations shown in Figure 5c. For the simulated cell with identical surface area for both planar electrodes,  $\Delta\psi_P(t)$  was much smaller than  $\Delta\psi_C(t)$  since the faradaic charge storage yielded a larger capacitance than EDL charge storage. This explains why the large changes in  $d\Delta\psi_P/dt$  resulted in relatively small kinks in the cell potential  $\psi_s(t)$  (Figure 5a) compared to those observed for experimental cells with oversized porous carbon electrodes (Figure 1a). In the capacitive regime, the temporal evolution of  $\Delta\psi_P(t)$  was linear and symmetric around the transition from charging to discharging. These distinct asymptotic behaviors suggest that measuring the potential of the pseudocapacitive electrode relative to a reference electrode provides a practical way to assess whether it is operating in the faradaic or the capacitive regime.

Figure 5d establishes that, for the carbon electrode, the evolution of  $\Delta\psi_C(t)$  was symmetric around the transition from charging to discharging. Its variation was nearly linear, but the slope  $|d\psi_s/dt|$  did vary noticeably over the cycle, indicating that the EDL differential capacitance  $C_{s,diff}$  was not constant, as assumed by many existing models.<sup>36-41</sup> Here,  $\Delta\psi_C(t)$  was also self-similar and identical for all values of  $j_s$  when plotted as a function of  $t/t_c$ . This implies that there was no ion diffusion limitation in the electrolyte, even at large values of  $j_s$  when  $j_F$  was negligible. Thus, the changes in the cell potential  $\psi_s(t)$  with increasing  $j_s$  were associated solely with changes on the pseudocapacitive side of the cell. Here, the carbon electrode had zero

net charge and  $\Delta\psi_C = 0 \text{ V}$  at the end of each cycle with fixed  $\Delta q_s$ , as it exchanged charge only with the external circuit.

*Ion concentrations in the electrolyte.*— Figure 6 shows the predicted concentrations of (a)  $\text{Li}^+$  cations  $c_{1,E}(-L + H, t)$  and (b)  $\text{ClO}_4^-$  anions  $c_{2,E}(-L + H, t)$  at the Stern/diffuse layer interface near the pseudocapacitive electrode as functions of dimensionless time  $t/t_c$  for different values of  $j_s$  and  $t_c$  under oscillatory steady state. Similarly, Figures 6c and 6d respectively show the predicted cation  $c_{1,E}(L - H, t)$  and anion  $c_{2,E}(L - H, t)$  concentrations at the Stern/diffuse layer interface near the carbon electrode. Here, ion concentrations larger than the bulk concentrations  $c_{1,E,\infty} = c_{2,E,\infty}$  correspond to the presence of an EDL.

Figures 6a and 6b indicate that EDLs formed near the pseudocapacitive electrode for all  $j_s$  considered. However, the concentrations of both  $\text{Li}^+$  and  $\text{ClO}_4^-$  remained closer to their bulk concentrations  $c_{1,E,\infty} = c_{2,E,\infty} = 1 \text{ mol L}^{-1}$  as  $j_s$  decreased. In fact, in the faradaic regime, the deviations from the bulk concentrations did not result in a large error in the value of  $\eta_F(t)$  predicted by Equation 31 and derived by assuming  $c_{1,E}(-L + H, t) \approx c_{2,E}(-L + H, t) \approx c_{1,E,\infty} = c_{2,E,\infty}$ . In this regime, an EDL of  $\text{Li}^+$  formed near the pseudocapacitive electrode during the charging step and an EDL of  $\text{ClO}_4^-$  during the discharging step. As  $j_s$  increased, the formation of the  $\text{Li}^+$  EDL near the pseudocapacitive electrode occurred later in the charging step. In the capacitive regime, an EDL consisting of  $\text{ClO}_4^-$  formed at the beginning and end of the cycle while a  $\text{Li}^+$  EDL formed briefly around the transition from charging to discharging (around  $t/t_c \approx n_c - 0.5$ ). In addition, the  $\text{Li}^+$  concentration  $c_{1,E}(-L + H, t)$  approached zero at the beginning and end of the cycle when  $\Delta\psi_H$  was positive and large. This resulted in a very small faradaic current density  $j_F$  (Figure 3a) as the exchange current density  $j_{F,0}$  vanished due to  $\text{Li}^+$  starvation (Equation 9). In both regimes, the sign of the electric field  $E(-L + H, t) = \Delta\psi_H(t)/H$  at the Stern/diffuse layer interface near the pseudocapacitive electrode determined which ion species formed the EDL. For  $\Delta\psi_{eq} = 0 \text{ V}$ ,  $E(-L + H, t)$  always had the same sign as the surface overpotential  $\eta(t)$  (Figure 5b). Positive  $\eta(t)$  and  $E(-L + H, t)$  corresponded to an EDL of  $\text{ClO}_4^-$  and negative  $\eta(t)$  and  $E(-L + H, t)$  to an EDL of  $\text{Li}^+$ . When they were equal to zero, the EDL vanished and both ion species were at their bulk concentrations, i.e.,  $c_{1,E}(-L + H, t) = c_{2,E}(-L + H, t) = c_{1,E,\infty} = c_{2,E,\infty}$ .

Figures 6c and 6d establish that the temporal evolutions of the ion concentrations near the carbon electrode were self-similar and were identical when plotted as functions of  $t/t_c$  for all current densities  $j_s$  and cycle periods  $t_c$  considered. This further confirms that ion transport in the electrolyte was not diffusion limited in the range of  $j_s$  considered. In addition, the results obtained near the carbon electrode resembled those observed in previous simulations of EDLCs.<sup>62</sup> Figure 6d indicates that, during the charging step, the concentration  $c_{2,E}(L - H, t)$  of the anion  $\text{ClO}_4^-$  increased until it reached its maximum value  $c_{2,E,max}$ , corresponding to the formation of an EDL of  $\text{ClO}_4^-$ .

*Effect of variable equilibrium potential drop  $\Delta\psi_{eq}$ .*— Figure 7 shows the numerically predicted (a) faradaic  $j_F(t)/j_s$  and (b) capacitive  $j_C(t)/j_s$  fractions of the total current density, (c) potential  $\Delta\psi_P(t)$  of the pseudocapacitive electrode relative to bulk electrolyte, and (d) cell potential  $\psi_s(t)$  as functions of dimensionless time  $t/t_c$  for  $S_{eq}$  equal to 0 V, 1 V, and 10.5 V. The selected cases with  $[j_s \text{ (mAcm}^{-2}\text{)}, t_c \text{ (ms)}] = [2, 30]$  and  $[256, 0.23]$  respectively corresponded to the faradaic and capacitive regimes previously identified for ideal faradaic behavior with  $S_{eq} = 0 \text{ V}$  (Figure 3). Figures 7a and 7b show that the evolutions of  $j_F/j_s$  and  $j_C/j_s$  for a given  $[j_s, t_c]$  were qualitatively similar for all values of  $S_{eq}$  considered. For  $j_s = 256 \text{ mA cm}^{-2}$ , the capacitive current density  $j_C(t)$  dominated (capacitive regime) and was not significantly affected by changes in  $S_{eq}$ . The changes in  $j_F(t)/j_s$  and the corresponding small changes in  $j_C(t)/j_s$  can be attributed to the fact that the  $\text{Li}^+$  concentration  $c_{1,E}(-L + H, t)$  at the Stern/diffuse layer interface near the

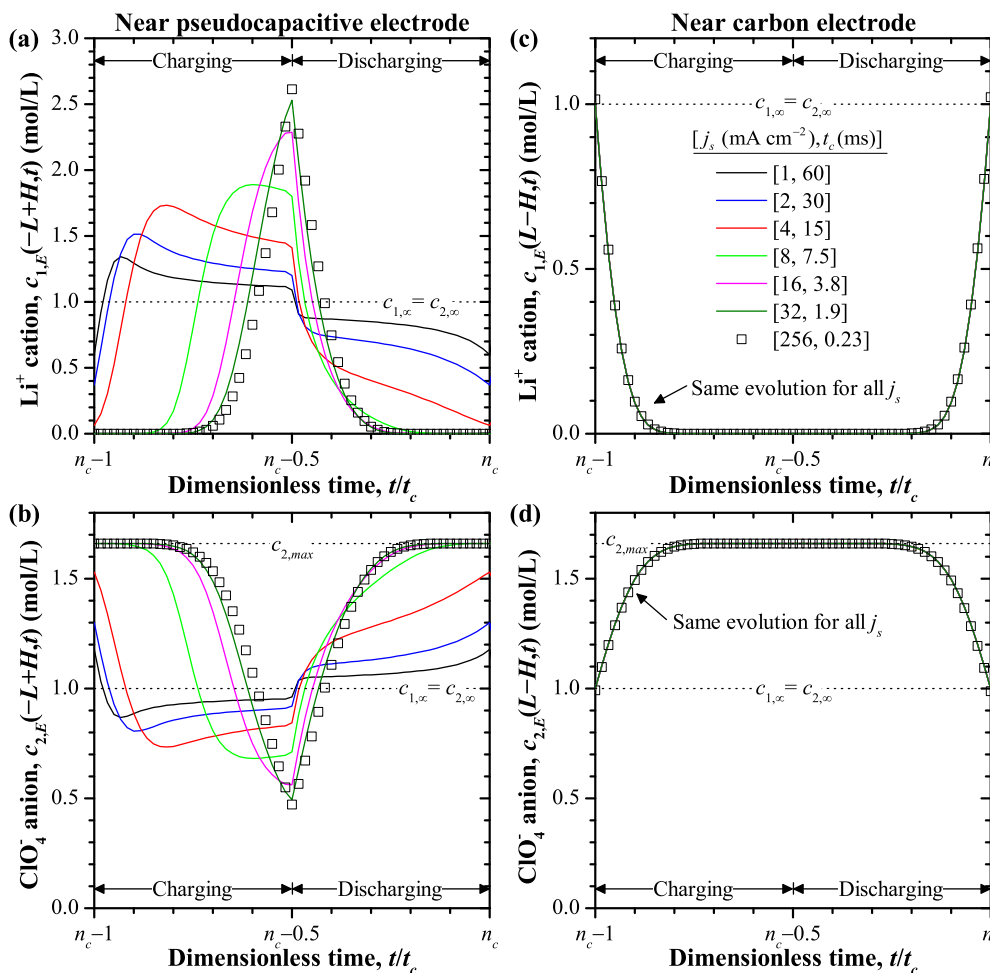


**Figure 6.** Predicted concentrations of (a)  $\text{Li}^+$  cation  $c_{1,E}(-L+H,t)$  and (b)  $\text{ClO}_4^-$  anion  $c_{2,E}(-L+H,t)$  at the Stern/diffuse layer interface near the pseudocapacitive electrode as well as concentrations of (c)  $\text{Li}^+$   $c_{1,E}(L-H,t)$  and (d)  $\text{ClO}_4^-$   $c_{2,E}(L-H,t)$  at the Stern/diffuse layer interface near the carbon electrode as functions of dimensionless time  $t/t_c$  over one cycle at oscillatory steady state for different values of  $j_s$  and  $t_c$  such that  $\Delta q_s = j_s t_c / 2 = 0.3 \text{ C m}^{-2}$ .

pseudocapacitive electrode increased with increasing  $S_{eq}$  (not shown). As a result, the  $\text{Li}^+$  starvation observed at the beginning and end of the cycle in Figure 6 and causing very small  $j_F(t)$  vanished for  $S_{eq} = 10.5 \text{ V}$ . For  $j_s = 2 \text{ mA cm}^{-2}$ , the faradaic fraction of the total current  $|j_F(t)/j_s|$  decreased with increasing  $S_{eq}$ . This can be attributed to the fact that non-zero rate of change  $d\Delta\psi_{eq}/dt$  resulted in non-zero capacitive current density  $j_C$ . Rearranging Equation 29 and combining it with  $j_{im}(t) = j_F(t) + j_C(t)$  yields

$$j_C(t) = j_{im}(t) - j_F(t) = \frac{\epsilon_0 \epsilon_r}{H} \left[ \frac{d\eta(t)}{dt} + \frac{d\Delta\psi_{eq}(t)}{dt} \right]. \quad [34]$$

After substitution for  $\Delta\psi_{eq}$  based on Equations 25 and 26,  $j_F$  can be expressed as

$$j_F(t) = \frac{j_{im}(t) - \frac{\epsilon_0 \epsilon_r}{H} \frac{d\eta(t)}{dt}}{1 + \frac{\epsilon_0 \epsilon_r S_{eq} A_P}{H c_{1,P,max} z_{1,E} F}}. \quad [35]$$

As a result,  $S_{eq} > 0 \text{ V}$  prevented the hybrid pseudocapacitor from reaching the faradaic limit  $j_F(t) \approx j_{im}(t)$  even when  $d\eta(t)/dt$  was negligible. For the cases considered in the present study and  $d\eta/dt \approx 0$ , Equation 35 predicted  $j_F = 0.93 j_{im}$  for  $S_{eq} = 1 \text{ V}$  and  $j_F = 0.56 j_{im}$  for  $S_{eq} = 10.5 \text{ V}$ . This agrees well with the numerical predictions shown in Figure 7a. Figure 7c shows that, for  $j_s = 2 \text{ mA cm}^{-2}$ , the potential drop  $\Delta\psi_P(t)$  across the pseudocapacitive electrode half-cell decreased with increasing  $S_{eq}$ . For  $S_{eq} = 10.5 \text{ V}$ ,  $\Delta\psi_P(t)$  had

a significant slope  $d\Delta\psi_P(t)/dt$  throughout the cycle and qualitatively resembled that measured experimentally (Figure 1a). Figure 7d shows that this resulted in the potential window  $\Delta\psi_s$  increasing and thus the integral capacitance  $C_{s,int}$  decreasing with increasing  $S_{eq}$  for  $j_s = 2 \text{ mA cm}^{-2}$ .

It is interesting to note that experimental measurements for  $\text{MnO}_2$  electrodes showed smaller values of  $S_{eq}$  for thin-film electrodes than for thick porous electrodes.<sup>31</sup> The present results suggest that this would cause smaller faradaic current and smaller capacitances for thick porous electrodes compared with thin films. Indeed, smaller capacitance for thicker electrodes has been observed experimentally.<sup>79</sup> It is also noteworthy that the predicted  $j_F$  and  $j_C$  corresponding to ideal faradaic behavior with  $S_{eq} = 0 \text{ V}$  were quite close to those for  $S_{eq} = 1 \text{ V}$ , approximately the value measured for thin  $\text{MnO}_2$  films.<sup>31</sup> This suggests that constant  $\Delta\psi_{eq}$  is a reasonable first approximation for simulating thin electrodes.

**Charging by  $\text{Li}^+$  deintercalation.**— As previously mentioned, for some hybrid pseudocapacitors, such as those using  $\text{MnO}_2$  positive electrodes, charging corresponds to deintercalation of the cation. This can be implemented by replacing Equation 14 with

$$j_{im}(t) = \begin{cases} j_s & \text{for charging } (n_c - 1)t_c \leq t < (n_c - 1/2)t_c \\ -j_s & \text{for discharging } (n_c - 1/2)t_c \leq t < n_c t_c. \end{cases} \quad [36]$$

In addition, a significant initial concentration of intercalated  $\text{Li}^+$   $c_{1,P,0} = 1 \text{ mol L}^{-1}$  was used in order to accommodate the initial

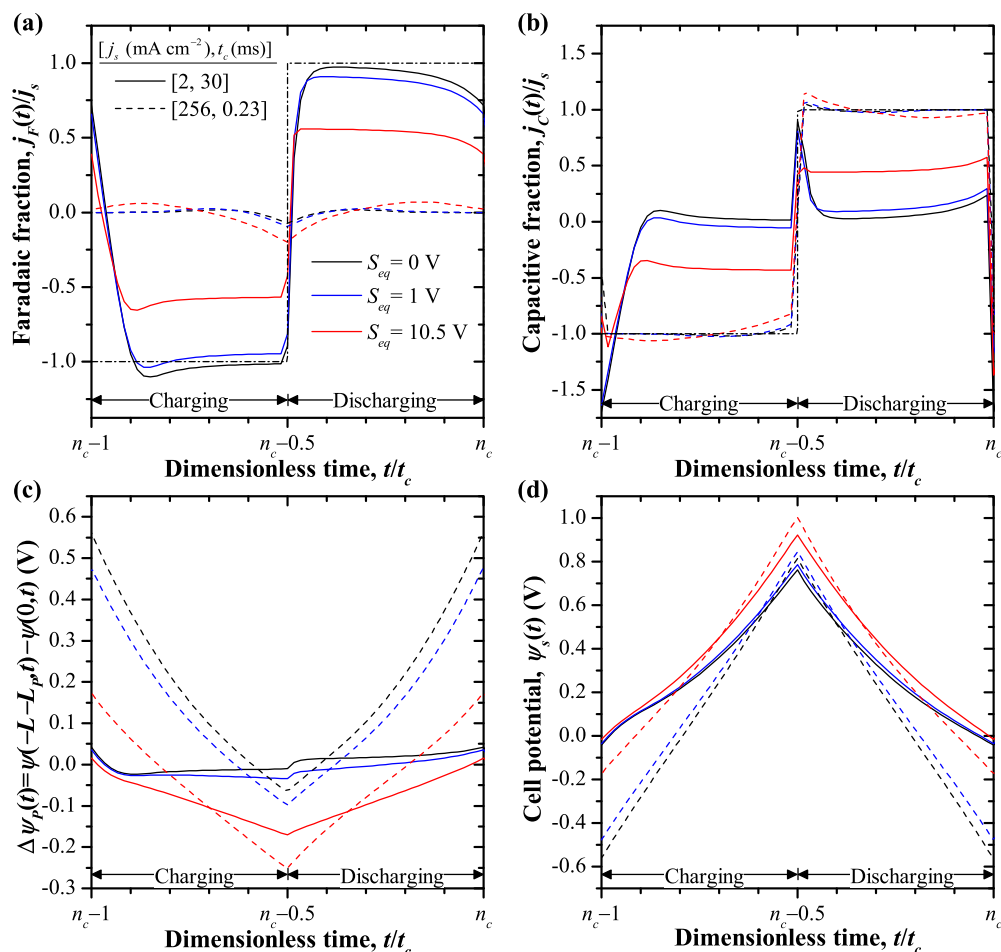


**Figure 7.** Predicted (a) faradaic  $j_F(t)/j_s$  and (b) capacitive  $j_C(t)/j_s$  fractions of the total current density, (c) potential  $\Delta\psi_p(t)$  of the pseudocapacitive electrode relative to bulk electrolyte, and (d) cell potential  $\psi_s(t)$  as functions of dimensionless time  $t/t_c$  for  $S_{eq} = 0, 1,$  and  $10.5$  V under galvanostatic cycling. The two selected cases  $[j_s, t_c]$  corresponded to the faradaic and capacitive regimes identified for  $S_{eq} = 0$  V and satisfying  $\Delta q_s = j_s t_c / 2 = 0.3$  C m $^{-2}$ .

deintercalation of  $\text{Li}^+$ , as done during material synthesis of  $\text{MnO}_2$  electrodes.<sup>16,19</sup> Here also,  $S_{eq}$  was taken as  $S_{eq} = 0$  V corresponding to ideal faradaic behavior.

Figure 8 shows (a) the faradaic  $j_F(t)/j_s$  and (b) capacitive  $j_C(t)/j_s$  fractions of the imposed current as well as (c) the surface overpotential  $\eta(t)$  and (d) the cell potential  $\psi_s(t) = \Delta\psi_p(t) - \Delta\psi_c(t)$  for the hybrid pseudocapacitor charged by deintercalation. Figures 8a and 8b indicate that the previously observed faradaic and capacitive regimes also occurred for charging by deintercalation. In addition, Figure 8c shows that the numerically predicted overpotential  $\eta$  agreed well with the analytical predictions  $\eta_F$  and  $\eta_C$  (Equations 31 to 33). Here,  $|\eta_F|$  reached a maximum at the end of the charging step when  $c_{1,p,F}$  was minimum. Moreover,  $|\eta_C|$  was large and positive around the transition from charging to discharging. This resulted in  $\text{Li}^+$  starvation in the electrolyte, i.e.,  $c_{1,E}(-L + H, t) \approx 0$  mol L $^{-1}$  (not shown), and  $j_F \approx 0$  mA cm $^{-2}$  at this time rather than around the transition from discharging to charging as previously observed (Figure 3a). Figure 8d shows that the cell potential evolution  $\psi_s(t)$  had similar qualitative behavior to that observed for charging by intercalation (Figure 5a). In the faradaic regime, it qualitatively resembled experimental measurements (Figure 1b). The potential window  $\Delta\psi_s$  was smaller than that for the same values of  $j_s$  and  $t_c$  when charging by intercalation. Thus, charging by deintercalation, with the present planar electrodes, resulted in a larger integral capacitance  $C_{s,int}$ . At the pseudocapacitive electrode,  $|\eta_F|$  remained relatively small because  $c_{1,p,F}$  remained relatively large ( $>0.38$  mol L $^{-1}$ ). At the carbon electrode, the EDL was formed by the smaller  $\text{Li}^+$  ions rather than  $\text{ClO}_4^-$ , leading to larger maximum concentration  $c_{1,E,max}$  and thus to larger EDL capacitance.<sup>62</sup>

Here also, a faradaic “kink” in  $\psi_s(t)$  was evident at the beginning of both the charging and discharging steps. However, it was more prominent at the beginning of the discharging step. This can be attributed to the fact that  $|\eta_F|$  was maximum at the transition from charging to discharging, requiring a relatively large change in  $\eta$  before the faradaic current could become dominant again.

*Hybrid pseudocapacitors with porous electrodes.*— The present study considered only planar electrodes while practical hybrid pseudocapacitors use porous electrodes. First, our simulations based on planar electrodes qualitatively reproduced experimental cell potential features measured on hybrid pseudocapacitors with porous electrodes. This suggests that the model captures the key physical phenomena occurring in realistic electrode geometries. However, accounting for porous electrodes is necessary (i) to provide quantitative predictions of actual hybrid pseudocapacitors and/or (ii) to investigate the effects of electrode morphology. Second, the present model could be extended to porous electrodes using various approaches. It could be employed to directly simulate transport in ordered three-dimensional porous electrodes. This approach could yield valuable information about the effect of the electrode material architecture on the electrochemical transport and provide design rules. New electrodes and hybrid pseudocapacitor devices designed using such insights may enable expansion of the faradaic regime to achieve larger capacitance and energy density. However, it would be computationally very costly and time consuming. In addition, insights and analytical expressions obtained from the present detailed model and from planar-electrode simulations could be used to develop volume-averaged continuum

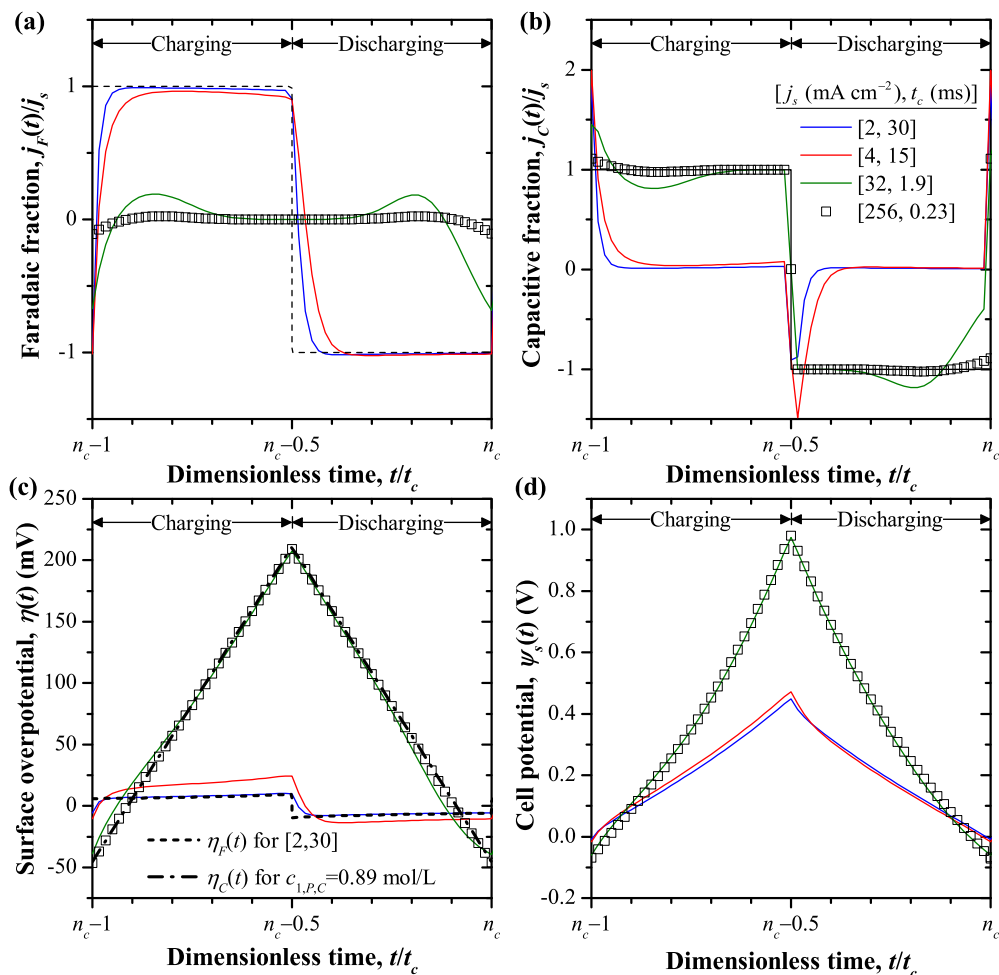


**Figure 8.** Predicted (a) the faradaic  $j_F(t)/j_s$  and (b) capacitive  $j_C(t)/j_s$  fractions of the imposed current as well as (c) the surface overpotential  $\eta(t)$  and (d) the cell potential  $\psi_s(t) = \Delta\psi_P(t) - \Delta\psi_C(t)$  for the hybrid pseudocapacitor charged by deintercalation for various  $[j_s, t_c]$  satisfying  $\Delta q_s = j_s t_c / 2 = 0.3 \text{ C m}^{-2}$ .

models, similar to those described earlier but accounting for the effects of EDL formation. This approach could enable the simulation of realistic hybrid pseudocapacitor devices. Such models could identify operating conditions that maximize the capacitance of existing devices. Note that in all cases, the continuum model is valid for pore or particle size larger than 5 nm when dielectric and transport properties can be defined in the framework of continuum theory. For pores or particles smaller than 1-5 nm, multiscale coupling of the present continuum model with (i) quantum mechanical models, such as density functional theory (DFT), and/or (ii) atomistic models, such as MD simulations, could be formulated for quantitative predictions. However, this falls outside the scope of the present study.

### Conclusions

The present study investigated the electrochemical transport phenomena occurring inside hybrid pseudocapacitors under galvanostatic cycling using a rigorous physical model accounting for coupled EDL formation and faradaic reactions. Detailed numerical simulations were performed for a hybrid pseudocapacitor with planar electrodes under various current densities and cycle periods. First, two asymptotic regimes were identified: (i) a faradaic regime dominated by redox reactions at small  $j_s$  and slow charging and (ii) a capacitive regime dominated by EDL formation under large  $j_s$  and fast charging. In these regimes, simple analytical expressions were derived for the  $\text{Li}^+$  concentration intercalated in the pseudocapacitive electrode and for the surface overpotential as functions of time. The surface overpotential was important in determining whether EDL or faradaic charge

storage dominated. The larger its value at the charging/discharging transitions, the smaller the faradaic fraction of the charge storage. Second, the predicted cell potentials resembled those reported experimentally. In particular, characteristic “kinks” occurred immediately after charging/discharging transitions and were attributed to brief periods of EDL charge storage as the surface overpotential and ion concentrations adjusted to the new direction of the current, before the faradaic charge storage became dominant again. Finally, variation of the equilibrium potential drop  $\Delta\psi_{eq}$  with the state of charge negatively affected the faradaic charge storage and prevented the device from operating in the faradaic regime, even at small current, thus reducing its capacitance. Overall, this study indicates that accounting for coupling between EDL formation and faradaic reactions is essential for reproducing and interpreting experimental measurements. The numerical model and the derived analytical expressions provide useful tools for optimizing hybrid pseudocapacitor performance by developing design rules and/or improving the predictions of volume-averaged models. They can also serve as a foundation for physics-based modeling of other quantities of interest, such as predicting internal heat generation rates in order to develop thermal management strategies.

### Acknowledgment

This material is based upon work supported by the National Science Foundation Graduate Research Fellowship under Grant No. DGE-1144087 and as part of the Molecularly Engineered Energy Materials, an Energy Frontier Research Center funded by the U.S.

Department of Energy, Office of Science, Office of Basic Energy Sciences under Award Number DE-SC0001342.

## References

- B. Conway, *Electrochemical Supercapacitors: Scientific Fundamentals and Technological Applications*, Kluwer Academic/Plenum Publishers, New York, NY, 1999.
- US Department of Energy, Basic Research Needs for Electrical Energy Storage: Report of the Basic Energy Sciences Workshop for Electrical Energy Storage, Tech. rep., Office of Basic Energy Sciences, DOE (2007). URL <http://www.osti.gov/accomplishments/documents/fullText/ACC0330.pdf>
- T. Pandolfo, V. Ruiz, S. Sivakkumar, and J. Nerkar, *General properties of electrochemical capacitors*, in: F. Béguin and E. Frackowiak (Eds.), *Supercapacitors: Materials, Systems, and Applications*, Wiley-VCH Verlag, Weinheim, Germany, 2013, Ch. 2, pp. 69.
- C. A. Vincent and B. Scrosati (Eds.), *Modern Batteries: An Introduction to Electrochemical Power Sources*, 2nd Edition, Butterworth-Heinemann, Burlington, MA, 2003.
- E. Frackowiak, *Electrode materials with pseudocapacitive properties*, in: F. Béguin and E. Frackowiak (Eds.), *Supercapacitors: Materials, Systems, and Applications*, Wiley-VCH Verlag, Weinheim, Germany, 2013, Ch. 6, pp. 207.
- P. Simon, Y. Gogotsi, and B. Dunn, "Where do batteries end and supercapacitors begin?," *Science*, **343**, 1210 (2014).
- J. W. Kim, V. Augustyn, and B. Dunn, "The effect of crystallinity on the rapid pseudocapacitive response of Nb<sub>2</sub>O<sub>5</sub>," *Advanced Energy Materials*, **2**, 141 (2012).
- V. Augustyn, J. Come, M. A. Lowe, J. W. Kim, P.-L. Taberna, S. H. Tolbert, H. D. Abruña, P. Simon, and B. Dunn, "High-rate electrochemical energy storage through Li<sup>+</sup> intercalation pseudocapacitance," *Nature Materials*, **12**, 518 (2013).
- L. Kong, C. Zhang, S. Zhang, J. Wang, R. Cai, C. Lv, W. Qiao, L. Ling, and D. Long, "High-power and high-energy asymmetric supercapacitors based on Li<sup>+</sup> intercalation into a T-Nb<sub>2</sub>O<sub>5</sub>/graphene pseudocapacitive electrode," *Journal of Materials Chemistry A*, **2**(42), 17962 (2014).
- H.-L. Girard, H. Wang, A. d'Entremont, and L. Pilon, "Physical interpretation of cyclic voltammetry for hybrid pseudocapacitors," *Journal of Physical Chemistry C*, **119**(21), 11349 (2015).
- H. Wang and L. Pilon, "Reply to comments on "Intrinsic limitations of impedance measurements in determining electric double layer capacitances," by H. Wang and L. Pilon [Electrochimica Acta 63 (2012) 55] *Electrochimica Acta*, **76**, 529 (2012).
- J. Come, V. Augustyn, J. W. Kim, P. Rozier, P.-L. Taberna, P. Gogotsi, J. W. Kong, B. Dunn, and P. Simon, "Electrochemical kinetics of nanostructured Nb<sub>2</sub>O<sub>5</sub> electrodes," *Journal of the Electrochemical Society*, **161**, A718 (2014).
- K. Brezesinski, J. Wang, J. Haetge, C. Reitz, S. O. Steinmueller, S. H. Tolbert, B. M. Smarsly, B. Dunn, and T. Brezesinski, "Pseudocapacitive contributions to charge storage in highly ordered mesoporous group V transition metal oxides with iso-oriented layered nanocrystalline domains," *Journal of the American Chemical Society*, **132**, 6982 (2010).
- X. Wang, G. Li, Z. Chen, V. Augustyn, X. Ma, G. Wang, B. Dunn, and Y. Lu, "High-performance supercapacitors based on nanocomposites of Nb<sub>2</sub>O<sub>5</sub> nanocrystals and carbon nanotubes," *Advanced Energy Materials*, **1**, (2011) 1089.
- D. Bélanger, T. Brousse, and J. W. Long, "Manganese oxides: Battery materials make the leap to electrochemical capacitors," *The Electrochemical Society Interface*, **17**, 49 (2008).
- M. Toupin, T. Brousse, and D. Bélanger, "Charge storage mechanism of MnO<sub>2</sub> electrode used in aqueous electrochemical capacitor," *Chemistry of Materials*, **16**, 3184 (2004).
- T. Cottineau, M. Toupin, T. Delahaye, T. Brousse, and D. Bélanger, "Nanostructured transition metal oxides for aqueous hybrid electrochemical supercapacitors," *Applied Physics A*, **82**(4), 599 (2006).
- T. Brousse, P.-L. Taberna, O. Crosnier, R. Dugas, P. Guillemet, Y. Scudeller, Y. Zhou, F. Favier, D. Bélanger, and P. Simon, "Long-term cycling behavior of asymmetric activated carbon/MnO<sub>2</sub> aqueous electrochemical supercapacitor," *Journal of Power Sources*, **173**(1), 633 (2007).
- Y.-G. Wang and Y.-Y. Xia, "Hybrid aqueous energy storage cells using activated carbon and lithium-intercalated compounds I. the C/LiMn<sub>2</sub>O<sub>4</sub> system," *Journal of The Electrochemical Society*, **153**, A450 (2006).
- M. S. Hong, S. H. Lee, and S. W. Kim, "Use of KCl aqueous electrolyte for 2 V manganese oxide/activated carbon hybrid capacitor," *Electrochemical and Solid-State Letters*, **5**(10), A227 (2002).
- E. Lim, H. Kim, C. Jo, J. Chun, K. Ku, S. Kim, H. I. Lee, I.-S. Nam, S. Yoon, K. Kang, and J. Lee, "Advanced hybrid supercapacitor based on a mesoporous niobium pentoxide/carbon as high-performance anode," *ACS Nano*, **8**(9), 8968 (2014).
- E. Lim, C. Jo, H. Kim, M.-H. Kim, Y. Mun, J. Chun, Y. Ye, J. Hwang, K.-S. Ha, K. C. Roh, K. Kang, S. Yoon, and J. Lee, "Facile synthesis of Nb<sub>2</sub>O<sub>5</sub>@carbon core-shell nanocrystals with controlled crystalline structure for high-power anodes in hybrid supercapacitors," *ACS Nano*, **9**(7), 7497 (2015).
- A. Bard and L. Faulkner, *Electrochemical Methods: Fundamentals and Applications*, John Wiley & Sons, New York, NY, 2001.
- V. Bagotsky, *Fundamentals of Electrochemistry*, John Wiley & Sons, Hoboken, NJ, 2006.
- J. S. Newman and K. E. Thomas-Alyea, *Electrochemical Systems*, 3rd Edition, John Wiley & Sons, Hoboken, NJ, 2004.
- M. S. Kilic, M. Z. Bazant, and A. Ajdari, "Steric effects in the dynamics of electrolytes at large applied voltages. II. Modified Poisson-Nernst-Planck equations," *Physical Review E*, **75**(2), 021503 (2007).
- B. E. Conway, "Transition from supercapacitor to battery behavior in electrochemical energy storage," *Journal of the Electrochemical Society*, **138**(6), 1539 (1991).
- B. E. Conway, V. Birss, and J. Wojtowicz, "The role and utilization of pseudocapacitance for energy storage by supercapacitors," *Journal of Power Sources*, **66**, 1 (1997).
- Y. Zhang and H. Yang, "Modeling and characterization of supercapacitors for wireless sensor network applications," *Journal of Power Sources*, **196**(8), 4128 (2011).
- R. H. Nilson, M. T. Brumbach, and B. C. Bunker, "Modeling the electrochemical impedance spectra of electroactive pseudocapacitor materials," *Journal of The Electrochemical Society*, **158**(6), A678 (2011).
- P. Guillemet, T. Brousse, O. Crosnier, Y. Dandeville, L. Athouel, and Y. Scudeller, "Modeling pseudo capacitance of manganese dioxide," *Electrochimica Acta*, **67**, 41 (2012).
- J. F. Rubinson and Y. P. Kayinamura, "Charge transport in conducting polymers: insights from impedance spectroscopy," *Chemical Society Reviews*, **38**, 3339 (2009).
- M. Z. Bazant, K. Thornton, and A. Ajdari, "Diffuse-charge dynamics in electrochemical systems," *Physical review E*, **70**(2), 021506 (2004).
- K. T. Chu and M. Z. Bazant, "Nonlinear electrochemical relaxation around conductors," *Physical Review E*, **74**(1), 011501 (2006).
- L. H. Olesen, M. Z. Bazant, and H. Bruus, "Strongly nonlinear dynamics of electrolytes in large AC voltages," *Physical Review E*, **82**, 011501 (2010).
- C. Lin, J. A. Ritter, B. N. Popov, and R. E. White, "A mathematical model of an electrochemical capacitor with double-layer and faradaic processes," *Journal of the Electrochemical Society*, **146**(9), 3168 (1999).
- H. Kim and B. N. Popov, "A mathematical model of oxide/carbon composite electrode for supercapacitors," *Journal of the Electrochemical Society*, **150**(9), A1153 (2003).
- K. Somasundaram, E. Birgersson, and A. S. Mujumdar, "Analysis of a model for an electrochemical capacitor," *Journal of The Electrochemical Society*, **158**(11), A1220 (2011).
- H. Farsi and F. Gopal, "A mathematical model of nanoparticulate mixed oxide pseudocapacitors; Part II: the effects of intrinsic factors," *Journal of Solid State Electrochemistry*, **15**(1), 115 (2011).
- S. Devan, V. R. Subramanian, and R. E. White, "Transient analysis of a porous electrode," *Journal of The Electrochemical Society*, **152**(5), A947 (2005).
- J. A. Staser and J. W. Weidner, "Mathematical modeling of hybrid asymmetric electrochemical capacitors," *Journal of The Electrochemical Society*, **161**(8), E3267 (2014).
- H. Farsi and F. Gopal, "A mathematical model of nanoparticulate mixed oxide pseudocapacitors; Part I: model description and particle size effects," *Journal of Solid State Electrochemistry*, **13**, 433 (2009).
- Y. Liu, F. Zhou, and V. Ozolins, "Ab initio study of the charge-storage mechanisms in RuO<sub>2</sub>-based electrochemical ultracapacitors," *The Journal of Physical Chemistry C*, **116**(1), 1450 (2011).
- V. Ozolins, F. Zhou, and M. Asta, "Ruthenium-based electrochemical supercapacitors: Insights from first-principles calculations," *Accounts of Chemical Research*, **46**(5), 1084 (2013).
- J. Kang, S.-H. Wei, K. Zhu, and Y.-H. Kim, "First-principles theory of electrochemical capacitance of nanostructured materials: Dipole-assisted subsurface intercalation of lithium in pseudocapacitive TiO<sub>2</sub> anatase nanosheets," *The Journal of Physical Chemistry C*, **115**(11), 4909 (2011).
- D. A. Tompsett, S. C. Parker, P. G. Bruce, and M. S. Islam, "Nanostructuring of β-MnO<sub>2</sub>: The important role of surface to bulk ion migration," *Chemistry of Materials*, **25**(4), 536 (2013).
- H. Ding, K. G. Ray, V. Ozolins, and M. Asta, "Structural and vibrational properties of α-MoO<sub>3</sub> from van der Waals corrected density functional theory calculations," *Physical Review B*, **85**(1), 012104 (2012).
- A. A. Lubimtshev, P. R. C. Kent, B. G. Sumpter, and P. Ganesh, "Understanding the origin of high-rate intercalation pseudocapacitance in Nb<sub>2</sub>O<sub>5</sub> crystals," *Journal of Materials Chemistry A*, **1**(47), 14951 (2013).
- G. Feng and P. T. Cummings, "Supercapacitor capacitance exhibits oscillatory behavior as a function of nanopore size," *The Journal of Physical Chemistry Letters*, **2**(22), 2859 (2011).
- Y. Shim and H. J. Kim, "Nanoporous carbon supercapacitors in an ionic liquid: A computer simulation study," *ACS nano*, **4**(4), 2345 (2010).
- H. Wang, J. Varghese, and L. Pilon, "Simulation of electric double layer capacitors with mesoporous electrodes: Effects of morphology and electrolyte permittivity," *Electrochimica Acta*, **56**, 6189 (2011).
- H. Wang and L. Pilon, "Mesoscale modeling of electric double layer capacitors with three-dimensional ordered structures," *Journal of Power Sources*, **221**, 252 (2013).
- C.-Y. Wang, "Fundamental models for fuel cell engineering," *Chemical Reviews*, **104**(10), 4727 (2004).
- C.-W. Wang and A. M. Sastry, "Mesoscale modeling of a Li-ion polymer cell," *Journal of the Electrochemical Society*, **154**(11), 1035 (2007).
- X. Xiao, W. Wu, and X. Huang, "A multi-scale approach for the stress analysis of polymeric separators in a lithium-ion battery," *Journal of Power Sources*, **195**(11), 7649 (2010).
- R. Chandrasekaran, A. Magasinski, G. Yushin, and T. F. Fuller, "Analysis of lithium insertion/deinsertion in a silicon electrode particle at room temperature," *Journal of the Electrochemical Society*, **157**(10), 1139 (2010).
- H. Wang, A. Thiele, and L. Pilon, "Simulations of cyclic voltammetry for electric double layers in asymmetric electrolytes: A generalized modified Poisson-Nernst-Planck model," *The Journal of Physical Chemistry C*, **117**, 18286 (2013).

58. P. M. Biesheuvel, M. van Soestbergen, and M. Z. Bazant, "Imposed currents in galvanic cells," *Electrochimica Acta*, **54**(21), 4857 (2009).
59. A. Frumkin, "Wasserstoffüberspannung und Struktur der Doppelschicht (Hydrogen overvoltage and the structure of the double layer)," *Zeitschrift für physikalische Chemie*, **164A**, 121 (1933).
60. S. R. Subramanian, V. Boovaragavan, V. Ramadesigan, and M. Arabandi, "Mathematical model reformulation for lithium-ion battery simulations: Galvanostatic boundary conditions," *Journal of the Electrochemical Society*, **156**(4), 260 (2009).
61. A. L. d'Entremont and L. Pilon, "First-principles thermal modeling of electric double layer capacitors under constant-current cycling," *Journal of Power Sources*, **246**, 887 (2014).
62. A. L. d'Entremont and L. Pilon, "Thermal effects of asymmetric electrolytes in electric double layer capacitors," *Journal of Power Sources*, **273**, 196 (2015).
63. A. Bonnefont, F. Argoul, and M. Z. Bazant, "Analysis of diffuse-layer effects on time-dependent interfacial kinetics," *Journal of Electroanalytical Chemistry*, **500**(1-2), 52 (2001).
64. J. Desilvestro and O. Haas, "Metal oxide cathode materials for electrochemical energy storage: A review," *Journal of the Electrochemical Society*, **137**, 5C (1990).
65. D. Zhang, B. N. Popov, and R. E. White, "Modeling lithium intercalation of a single spinel particle under potentiodynamic control," *Journal of the Electrochemical Society*, **147**(3), 831 (2000).
66. A. M. Colclasure and R. J. Kee, "Thermodynamically consistent modeling of elementary electrochemistry in lithium-ion batteries," *Electrochimica Acta*, **55**, 8960 (2010).
67. G. M. Goldin, A. M. Colclasure, A. H. Wiedemann, and R. J. Kee, "Three-dimensional particle-resolved models of li-ion batteries to assist the evaluation of empirical parameters in one-dimensional models," *Electrochimica Acta*, **64**, 118 (2012).
68. M. D. Chung, J. H. Seo, X. C. Zhang, and A. M. Sastry, "Implementing realistic geometry and measured diffusion coefficients into single particle electrode modeling based on experiments with single  $\text{LiMn}_2\text{O}_4$  spinel particles," *Journal of the Electrochemical Society*, **158**, 371 (2011).
69. A. G. Pandolfo and A. F. Hollenkamp, "Carbon properties and their role in supercapacitors," *Journal of Power Sources*, **157**, 11 (2006).
70. K. H. Radeke, K. O. Backhaus, and A. Swiatkowski, "Electrical conductivity of activated carbons," *Carbon*, **29**, 122 (1991).
71. A. Subrenat, J. N. Baléo, P. Le Cloirec, and P. E. Blanc, "Electrical behavior of activated carbon cloth heated by the Joule effect: Desorption application," *Carbon*, **39** 707 (2001).
72. T. R. Jow and J. P. Zheng, "Electrochemical capacitors using hydrous ruthenium oxide and hydrogen inserted ruthenium oxide," *Journal of the Electrochemical Society*, **145**, 49 (1998).
73. W. M. Haynes, T. J. Bruno, and D. R. Lide (Eds.) *CRC Handbook of Chemistry and Physics*, 94th Edition, CRC Press, Boca Raton, FL, 2013.
74. K. Nishikawa, Y. Fukunaka, T. Sakka, Y. H. Ogata, and J. R. Selman, "Measurement of  $\text{LiClO}_4$  diffusion coefficient in propylene carbonate by Moiré pattern," *Journal of the Electrochemical Society*, **153**, A830 (2006).
75. J. Xu and G. C. Farrington, "A novel electrochemical method for measuring salt diffusion coefficients and ion transference numbers," *Journal of the Electrochemical Society*, **143**(2), L44 (1996).
76. J. Schiffer, D. Linzen, and D. U. Sauer, "Heat generation in double layer capacitors," *Journal of Power Sources*, **160**(1), 765 (2006).
77. Y. Dandeville, P. Guillemet, Y. Scudeller, O. Crosnier, L. Athouel, and T. Brousse, "Measuring time-dependent heat profiles of aqueous electrochemical capacitors under cycling," *Thermochemica Acta*, **526**, 1 (2011).
78. COMSOL, Inc., COMSOL Multiphysics Reference Manual, COMSOL 4.4 Edition (2013).
79. V. Augustyn, P. Simon, and B. Dunn, "Pseudocapacitive oxide materials for high-rate electrochemical energy storage," *Energy and Environmental Science*, **7** 1597 (2014).